Article

Compositionally Complex Perovskite Oxides for Solar Thermochemical Water Splitting

Dawei Zhang,[+] Héctor A. De Santiago,[+] Boyuan Xu, Cijie Liu, Jamie A. Trindell, Wei Li,* Jiyun Park, Mark A. Rodriguez, Eric N. Coker, Joshua D. Sugar, Anthony H. McDaniel, Stephan Lany, Liang Ma, Yi Wang, Gregory Collins, Hanchen Tian, Wenyuan Li, Yue Qi,* Xingbo Liu,* and Jian Luo*

Read Online

ACCESS | Metrics & More | Article Recommendations | SI Supporting Information

ABSTRACT: Solar thermochemical hydrogen (STCH) generation is a promising approach for eco-friendly H_2 production, but conventional STCH redox compounds cannot easily achieve desirable thermodynamic and kinetic properties and phase stability simultaneously due to a rather limited compositional space. Expanding from the nascent high-entropy ceramics field, this study explores a new class of compositionally complex perovskite oxides $(La_{0.8}Sr_{0.2})(Mn_{(1-x)/3}Fe_{(1-x)/3}Co_xAl_{(1-x)/3})O_3$ with new non-equimolar designs for STCH. In situ X-ray photoelectron spectroscopy shows preferential redox of Co. The extent of reduction increases, but the intrinsic kinetics decreases, with increasing Co content. Consequently, $(La_{0.8}Sr_{0.2})(Mn_{0.2}Fe_{0.2}Co_{0.4}Al_{0.2})O_3$ achieves an optimal thermodynamic and kinetic balance. The combination of a moderate enthalpy of reduction, a high entropy of reduction, and preferable surface oxygen exchange kinetics enables a maximum H_2 production of 89.97 $mmol\ mol_{oxide}^{-1}$ in a short 1 h redox duration. Entropy stabilization may contribute to the phase stability during redox cycling without phase transformation, which enables STCH production for >50 cycles under harsh interrupted conditions. The underlying redox mechanism is further elucidated by a density functional theory-based parallel Monte Carlo computation approach. This study suggests a new class of non-equimolar compositionally complex ceramics for STCH and thermochemical looping.
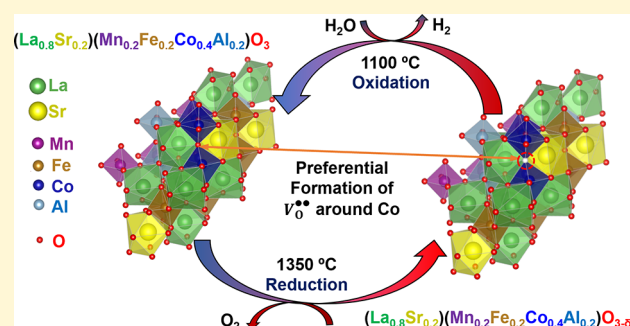
1. INTRODUCTION

Hydrogen has critical applications in modern industries and energy systems for future hydrogen economy.[1−5] To realize sustainable sunlight-driven water splitting and store intermittent solar energy, two-step solar thermochemical hydrogen production (STCH) has attracted considerable attention due to its capability of utilizing the full solar spectrum energy to generate fuels.[6−11] The two-step STCH process involves an endothermic reduction step at a high temperature (≥1200 °C) under low oxygen partial pressure (P_{O_2}) with a suitable non-stoichiometric metal oxide to release oxygen and a subsequent oxidation step via flowing steam to the reduced oxide at a relatively lower temperature (∼800−1100 °C). The most investigated non-stoichiometric metal oxide materials for STCH are undoped and doped ceria materials due to their phase stability and fast redox kinetics.[12−15] However, ceria ($CeO_{2−\delta}$, δ: oxygen non-stoichiometry) suffers from the requirement of extremely high reduction temperatures (>1500 °C) to reach a small extent of reduction ($\Delta\delta \approx$ 0.03−0.06), challenging the design of suitable reactors.[14,16] The perovskite oxides ($ABO_{3−\delta}$) are considered as a promising alternative candidate to ceria for STCH as they have favorable merits including relative phase stability under large non-

stoichiometry redox swing, tunable defect chemistry with A/B site doping, and a large compositional space.[17,18] For instance, $Ca(Ti_{0.5}Mn_{0.5})O_3$[19] and $(La_{1-x}Sr_x)(Mn_{1-y}Al_y)O_3$[20] perovskites have been investigated for STCH. Even though perovskites can have much larger redox capacities ($\Delta\delta$ > 0.15), a longer reaction time (total dwell time for reduction and oxidation steps >2 h) is usually required to reach a fair H_2 production in the reports.[21−23] An understanding of the tradeoff between thermodynamic and kinetics properties is needed to optimize the perovskite composition to achieve high H_2 production within a short time (≤1 h). Additionally, many reported perovskite oxides were found to show gradual phase transformation forming secondary phases with reduced or little redox capability in short-term cycles,[21,24−34] which is detrimental to H_2 production cycling stability. Therefore, it

is desirable to enhance the phase stability of perovskite oxides against thermochemical redox cycles.

High-entropy ceramics (HECs) have been synthesized in several material families including rocksalt,[35,36] perovskite,[37] and fluorite[38−40] oxides, as well as other non-oxides such as borides,[41] carbides,[42] and silicides.[43] Notably, an equimolar polycation $(Fe_{0.25}Mg_{0.25}Co_{0.25}Ni_{0.25})O_x$ was reported for STCH undergoing reversible phase transformation between the spinel and rocksalt structure for 10 cycles.[44] However, the repetitive phase transformation is not desirable for long-term cycling stability, reversibility, and oxygen exchange kinetics due to its larger energy barrier. Fe was proposed as the redox active element, although the ex situ characterization in that work may not precisely track the instantaneous redox change and the redox center valence may subject to change in the quenching/cooling process. It remains unclear why a particular cation dominates the redox chemistry and what factors govern the priority of redox behavior in the HECs during the STCH process. Recently, compositionally complex ceramics (CCCs) have been introduced to broaden the field of HECs by including non-equimolar compositions that reduce the configurational entropy but allow more engineering space to improve the properties.[45,46] CCCs can provide additional tunability of the physical properties, *e.g.*, thermomechanical properties, in compositionally complex fluorite-based oxides.[47,48] Here, we hypothesize that a vast compositional space in compositionally complex perovskite oxides (CCPOs) will enable us to create a new class of stable STCH materials, where non-equimolar compositional designs can be leveraged to balance the thermodynamic and kinetic properties.

Herein, we designed a new class of medium- to high-entropy CCPOs for two-step STCH with the chemical formula $(La_{0.8}Sr_{0.2})(Mn_{(1−x)/3}Fe_{(1−x)/3}Co_xAl_{(1−x)/3})O_3$, denoted as "LS_MFC$_x$A" for brevity (Table 1). Unlike benchmark

Table 1. Compositions of CCPOs and Abbreviations

sample abbreviations	nominal composition	molecular weight (mol g^{-1})
LS_MFC$_{0.16}$A	$(La_{0.8}Sr_{0.2})(Mn_{0.28}Fe_{0.28}Co_{0.16}Al_{0.28})O_{3−\delta}$	224.65
LS_MFC$_{0.2}$A	$(La_{0.8}Sr_{0.2})(Mn_{0.267}Fe_{0.267}Co_{0.20}Al_{0.267})O_{3−\delta}$	225.22
LS_MFC$_{0.25}$A	$(La_{0.8}Sr_{0.2})(Mn_{0.25}Fe_{0.25}Co_{0.25}Al_{0.25})O_{3−\delta}$	225.82
LS_MFC$_{0.4}$A	$(La_{0.8}Sr_{0.2})(Mn_{0.2}Fe_{0.2}Co_{0.4}Al_{0.2})O_{3−\delta}$	227.78
LS_MFC$_{0.52}$A	$(La_{0.8}Sr_{0.2})(Mn_{0.16}Fe_{0.16}Co_{0.52}Al_{0.16})O_{3−\delta}$	229.34
LS_MFC$_{0.61}$A	$(La_{0.8}Sr_{0.2})(Mn_{0.13}Fe_{0.13}Co_{0.61}Al_{0.13})O_{3−\delta}$	230.51
LS_MFC$_{0.79}$A	$(La_{0.8}Sr_{0.2})(Mn_{0.07}Fe_{0.07}Co_{0.79}Al_{0.07})O_{3−\delta}$	232.85
LSC	$(La_{0.8}Sr_{0.2})CoO_3$	235.58

perovskite materials such as $La_{1−x}Sr_xCoO_3$[26,27,29,30] and $BaCe_xMn_{1−x}O_3$,[24] this LS_MFC$_x$A series of CCPOs did not show any phase transformation during the STCH redox cycling for $x < 0.61$ confirmed by X-ray diffraction. In this series, the thermodynamic properties ($\Delta\delta$) are enhanced with the increasing Co content, whereas the intrinsic kinetic properties (oxygen surface exchange coefficient) are decreased with the increasing Co content. LS_MFC$_{0.4}$A $((La_{0.8}Sr_{0.2})(Mn_{0.2}Fe_{0.2}Co_{0.4}Al_{0.2})O_3)$ showed the best balance between the thermodynamic and kinetic properties, rendering a high

hydrogen production of 89.97 mmol mol$_{oxide}^{-1}$ within a short 1 h duration at an optimized STCH condition. The in situ X-ray photoelectron spectroscopy indicated that Co dominated the redox behavior. Furthermore, Monte Carlo (MC) sampling based on density functional theory (DFT) was applied in this field to demonstrate that oxygen vacancies prefer to form on the Co octahedron position among all B-site metal octahedron positions and the valence change of Co is the most obvious. Furthermore, we found that the Co−O bond in the CCPO is substantially weakened in comparison to Mn−O, Al−O, and Fe−O bonds in their respective simple perovskites, rationalizing the experimental observations. Moreover, LS_MFC$_{0.4}$A exhibited phase stability and moderate cycling durability even after 51 cycles under very harsh interrupted cycling conditions involving startup heating and shutdown cooling, which simulates the real-world day−night cycle conditions for STCH. This work opens up a new direction to explore novel CCCs for STCH and provides a new computation paradigm for a mechanistic understanding of redox chemistries of STCH materials. The concept of design of CCCs may guide the future development of materials for other applications such as thermochemical looping, catalysis, and electrochemistry.

2. EXPERIMENTAL SECTION

2.1. Material Synthesis. The CCPO samples of LS_MFC$_x$A were prepared by solid-state reactions. The starting powders, La$_2$O$_3$ (99.99%), SrCO$_3$ (99.9%), MnO$_2$ (99.5%), Fe$_2$O$_3$ (99.99%), Co$_3$O$_4$ (99.9%), and Al$_2$O$_3$ (99.99%), were purchased from Alfa Aesar. The precursor powders were mixed based on the calculated stoichiometry and placed in a poly(methyl methacrylate) high-energy ball mill (HEBM) vial with endcaps and milling balls made by tungsten carbide. The vials were dry-milled for 100 min (SPEX 8000D, SPEX SamplePrep, USA). Then, the mixed powder was annealed in air at 1300 °C for 10 h to form the single perovskite phase. The synthesized powder was ground by a pestle and mortar and further annealed in air at 1350 °C for another 10 h to improve the homogeneity and single-phase purity of final products, similar to previous reports of solid-state synthesis of perovskite materials for STCH.[19,49] For all syntheses, the heating rate was 5 °C min^{-1} and natural furnace cooling (about 10 °C min^{-1}) was applied. In a typical synthesis batch, around 2 g of products was obtained.

2.2. Phase Characterization. The phases were determined by X-ray diffraction (XRD) using a Rigaku Miniflex with Cu Kα radiation with an operating voltage of 30 kV and a current of 15 mA. All XRD patterns were taken with 0.02° step size and 2 s dwell time. The Rietveld refinements were performed using GSAS-II software. The crystallographic information file (cif) of LaAlO$_3$ ($R\bar{3}c$) from Inorganic Crystal Structure Database (ICSD #92554) was used as a starting structure. In situ high-temperature X-ray diffraction (HT-XRD) was performed on a Scintag PAD X powder X-ray diffractometer employing a sealed tube Cu Kα X-ray source, an incident beam mirror optic, fixed receiving slits, and a Peltier-cooled germanium solid-state detector. The ancillary hot stage was a Buehler HTK 2400 furnace with a Pt/Rh heating strip and surround heater. The temperature of the hot stage was calibrated via thermal expansion of a known standard alumina material under the similar testing conditions to the samples. Sample powders were ground under methanol and coated onto single-crystal yttria stabilized zirconia (YSZ) substrates for loading onto the heating strip. Mass flow controllers provided controlled gas flow through the furnace chamber. The specimen in HT-XRD experiments was heated up from room temperature to 1350 °C in flowing He, and the spectra were recorded at different isotherm stages (about 30 min each) with an interval of 50 °C from 850 to 1350 °C. The isothermal duration at 1350 °C was 1 h. The XRD patterns of cooling segments in flowing He were recorded at different isotherm stages of 1200, 1050, 900, and 800 °C (about 30 min each).

Table 2. Summary of STCH Production Results of LS_MFC$_{0.4}$A under Different Testing Conditions[a]

condition #	flow rate (sccm)	T_{Ox} (°C)	t_{Re} (min)	t_{Ox} (min)	cumulative H$_2$ production (μmol g^{-1})/(mmol mol^{-1})	H$_2$O conversion extent (%)
C1	100	800	45	15	49/11.16	0.18
C2	100	1000	45	15	194/44.19	0.72
C3	100	1100	45	15	219/49.88	0.82
C4	100	1100	30	30	270/61.50	0.50
C5	100	1100	30	60	351/79.95	0.33
C6	200	1100	30	30	395/89.97	0.74

[a]The reduction was conducted at 1350 °C in N$_2$ and oxidation was performed in 40% steam with N$_2$ for all cases. Cumulative H$_2$ production is reported in two units.

Then, O$_2$ was introduced at 800 °C to oxidize the thermally reduced sample for 1 h.

2.3. Thermogravimetric Analysis (TGA). TGA was finished using a simultaneous thermal analyzer (NETZSCH STA 449 F3 Jupiter). For each test, 30 mg of sample was placed on an alumina crucible. The samples were heated up to 1350 °C with a 25 °C min^{-1} ramping rate and held isothermally for 45 min under ultrahigh-purity (UHP) Ar. Then, the sample was cooled down to 1100 °C with the same ramp rate under Ar. Subsequently, 21% O$_2$ balanced with Ar was introduced to reoxidize the sample. The mass loss curves of samples were calibrated by a blank crucible run. The loss of mass was calculated to obtain the extent of reduction ($\Delta\delta = \delta_{re} - \delta_{ox}$) for all samples. The first cycle usually exhibited activation behaviors due to surface adsorption. Thus, we chose to report the TGA results in the stabilized second cycle for all LS_MFC$_x$A samples for consistent comparison. The plateau during the reoxidation step of the first cycle was considered as the reference (δ_{ox}) for calculating $\Delta\delta$.

2.4. In Situ X-ray Photoelectron Spectroscopy (XPS). The in situ XPS work was accomplished with an AXIS Supra by Kratos Analytical. The synthesized LS_MFC$_{0.25}$A powder was pressed into a cylindrical pellet with 10 mm diameter and about 1.5 mm thickness with uniaxial hydraulic press. The pellet was sintered under 1350 °C for 12 h, and the surface was polished. The pellet specimen was put on the holder with a heater and transferred into the XPS chamber. We took the XPS spectra for the specimen under room temperature (25 °C) and then heated it up to 800 °C with a ramp rate of 5 °C min^{-1}. The specimen was held isothermally at 800 °C for 30 min to reach surface equilibrium, and then the XPS spectra were recorded at 800 °C. All spectra were calibrated by the C 1s peak at 284.8 eV for further data analysis.

2.5. Thermochemical Water Splitting. The STCH performances of materials were investigated using a homemade flow reactor (Figure S1). The powder (100 mg) was loaded into the middle point of a 24″ alumina tube with an outer diameter of 1/4″ and inner diameter of 3/16″ and loaded horizontally close to the thermocouple within a high-temperature programmable electric furnace (Carbolite HTF 17/5). The powder was evenly dispersed inside the tube located in the center heating zone to ensure the sufficient gas−solid contact and mass transfer, and there was a void over the powder to avoid a sudden pressure drop and powder blowing off. N$_2$ (UHP, Matheson) was used as a carrier gas, and the flow rate was controlled by a calibrated mass flow controller (Alicat Scientific). The steam (40 vol % H$_2$O) was generated using a water evaporator (humidity bottle, Fuel Cell Technologies, Inc.) with a target temperature of 85 °C and mixed with the N$_2$ gas by redirecting the flow of N$_2$ through a series of valves into the evaporator. The outlet was connected to a cold trap to condense and remove excess steam. To eliminate the inevitable errors of integrating the mass spectrometry response, the total H$_2$ production was collected with a gas sampling bag (Restek Multilayer Foil) for a given time. The H$_2$ concentration was measured by gas chromatography (GC-2014, Shimadzu), which was calibrated by a series of standard calibration H$_2$ gases (GASCO, Cal Gas Direct Inc.) with different concentrations balanced by N$_2$. The reduction temperature was fixed at 1350 °C. The oxidation temperatures were controlled at 800, 1000, 1100, and 1200 °C. The gas flow rates were controlled at 100 or 200 sccm. The detailed testing parameters can be found in Table 2 and Figure 3. Background H$_2$ production from

catalytic water thermolysis at different temperatures was subtracted from the total H$_2$ production, and only the H$_2$ production from the redox reaction was illustrated. To compare the kinetics and molar rate of gas production, some selected LS_MFC$_x$A compositions were tested in a stagnation flow reactor with mass spectrometry (MS) at Sandia National Laboratory (SNL). The oxygen uptake and release tests were also conducted at SNL. The testing condition has been described elsewhere.[20,24]

2.6. Measurement of Thermodynamic Properties. The thermodynamic properties of the optimal composition, LS_MFC$_{0.4}$A, was measured up to a maximum temperature of 1400 °C under six different pO_2 conditions ranging from 0.21 to 2.5 × 10^{-5} atm. Accordingly, ~300 mg of sample was loaded into the TGA chamber and pretreated at 1000 °C for 30 min under 21% O$_2$ balanced with UHP Ar with a heating and cooling rate of 30 K min^{-1} to remove any surface adsorbates from the sample. After the treatment, the temperature returned to 80 °C. Then, the sample was heated to the reference temperature of 1000 °C under 0.028 atm at a heating rate of 5 K min^{-1} and kept at 1000 °C for 1 h to equilibrate the sample. Then, either a continuous or stepwise procedure was used for high P_{O_2} and low P_{O_2} conditions, respectively. The continuous conditions were performed for $P_{O_2} \geq 0.028$ atm. Accordingly, the P_{O_2} was adjusted to the targeted value and the temperature was heated to 1400 °C, kept at 1400 °C for 1 h, cooled to 300 °C, and maintained at 300 °C for 1 h. Then, it was heated again to 1400 °C and kept under isothermal conditions for 1 h. The heating and cooling were under a heating/cooling rate of 2 K min^{-1}. Thereafter, the temperature was cooled to the reference temperature of 1000 °C at 5 K min^{-1} under the reference P_{O_2} of 0.028 atm and held at 1000 °C for 1 h to confirm if the equilibrium values between the two reference points were kept at the similar level. The stepwise conditions were performed for $P_{O_2} \leq$ 1.70 × 10^{-3} atm. Accordingly, the P_{O_2} was adjusted to the targeted value, and the temperature was increased to the initial testing condition at a ramp rate of 2 K min^{-1} and kept isothermally for 1−2 h until the sample was stabilized. Thereafter, the sample was treated in various isothermal conditions for 1−2 h with a temperature interval of 100 °C. The tested isothermal temperatures depended on the P_{O_2} up to 1400 °C. Thereafter, the temperature was cooled to the reference temperature of 1000 °C at 5 K min^{-1} under the reference P_{O_2} of 0.028 atm and held at 1000 °C for 1 h to confirm if the equilibrium values between the two reference points were kept at the similar level. The thermodynamic limit of equilibrium H$_2$ production was calculated using the obtained results (oxygen non-stoichiometry of LS_MFC$_{0.4}$A as a function of temperature and P_{O_2}) through an established method.[19,50,51] The thermodynamic limit of equilibrium H$_2$ production of LS_MFC$_{0.4}$A comes from the equilibrium change of $\Delta\delta = \delta_{re} - \delta_{ox}$, where δ_{re} and δ_{ox} represent the equilibrium δ values of thermochemical reduction (1350 °C under inert gas with 25 ppm P_{O_2}) and oxidative water splitting (1100 °C under 40 vol % H$_2$O balanced with inert gas), respectively.

2.7. Monte Carlo (MC) and Density Functional Theory (DFT) Calculations. To sample the massive structural space of CCPOs, we performed a density functional theory (DFT)-based parallel Monte Carlo (MC) study for both LS_MFCA bulk and vacancy
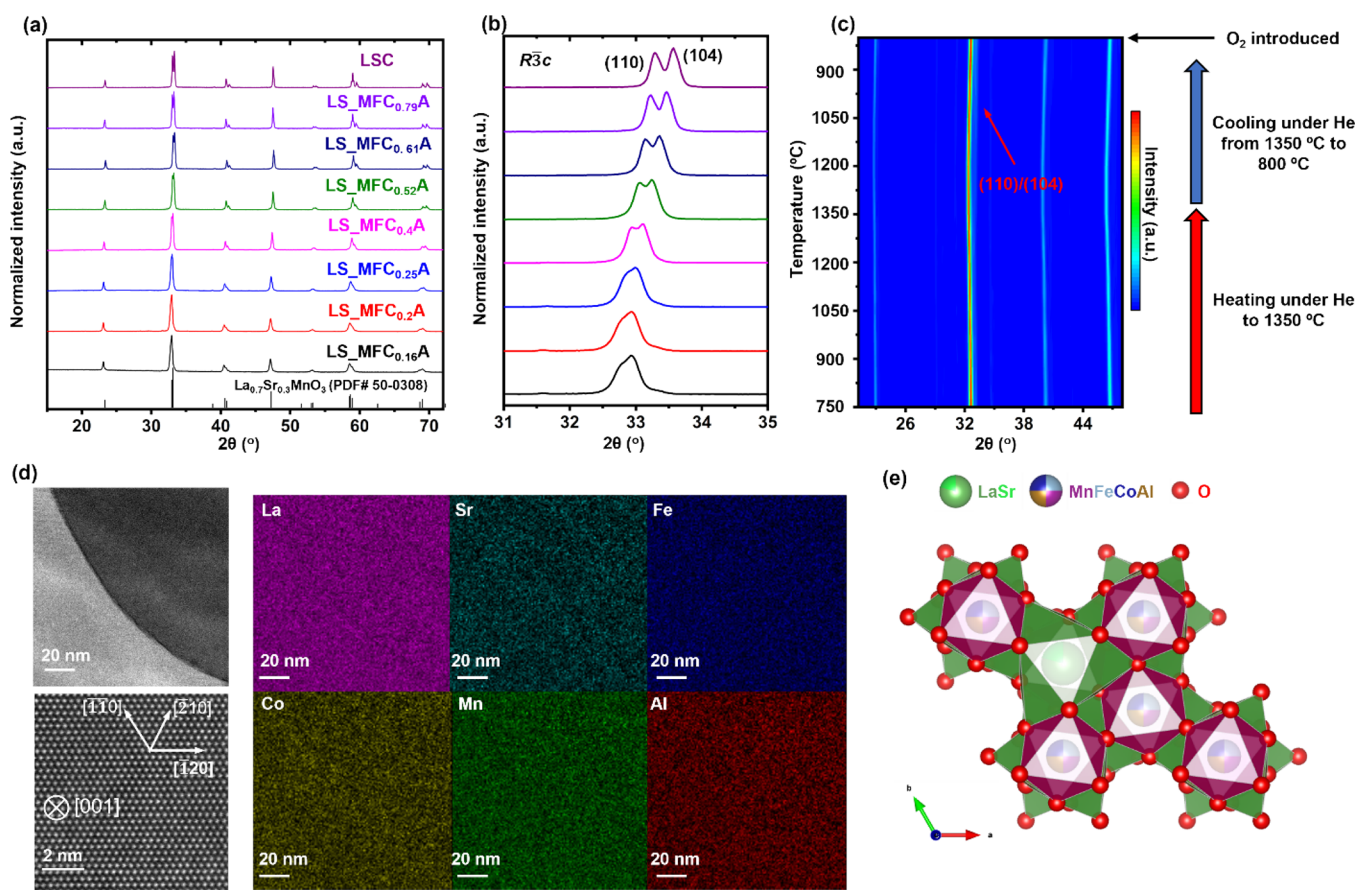
Figure 1. (a) XRD patterns of LS_MFC$_x$A (x = 0.16, 0.2, 0.25, 0.4, 0.52, 0.61, 0.79, and 1). (b) Splitting of (110) and (104) peaks showing the $R\bar{3}c$ rhombohedral structure. (c) HT-XRD pattern of LS_MFC$_{0.16}$A. The sample was heated from room temperature to 1350 °C under a He flow. There was no phase transformation or separation occurring in LS_MFC$_{0.16}$A under thermal reduction and oxidation conditions. (d) STEM HAADF images of LS_MFC$_{0.25}$A (with a grain boundary) and its nanoscale EDS elemental maps. (e) Schematic illustration of the corresponding crystal structure of LS_MFC$_{0.25}$A.

configurations to investigate the reduction mechanism. Four major initial perovskite structures, with space groups of $Pnma$, $R\bar{3}c$, and $Pm\bar{3}m$ as base structures, were used to generate randomly mixed 80-atom $(La_{0.75}Sr_{0.25})(Mn_{0.25}Fe_{0.25}Co_{0.25}Al_{0.25})O_3$ supercells (as the "seed"). Vacancy supercells were created by removing one of each nonequivalent oxygen from base structures before the cations were randomly mixed. Ten seed structures were generated for each symmetry. The MC workflow was built upon a framework developed for crystal structure prediction.[52] Each seed structure was evolved following a Monte Carlo "path", by first randomly switching the position or the magnetic moment of the two A-site elements or/and two out of the four B-site elements, relaxing with DFT calculations, and applying the Metropolis Monte Carlo acceptance criterion at 1600 K with the DFT computed energies. Here, 2600 accepted bulk and 3000 vacancy structures were saved and used for the analysis.

DFT calculations were performed using the Projector Augmented Wave (PAW) method[53] implemented in the Vienna Ab initio Simulation Package (VASP). The generalized gradient approximation (GGA) of Perdew, Burke, and Ernzerhof (PBE)[54] was used for the DFT exchange correlation functional. Hubbard U correction for 3d transition metal electrons was chosen to be 3.0 eV, and that for La 5d electrons was set to be 1.5 eV with an additional value for 4f electrons set to be 2.0 eV. The plane-wave cutoff energy was set to 320 eV, which is sufficient for the soft O pseudopotential, with a 2 × 2 × 2 Gamma point Monkhorst−Pack k-point meshes. Initial magnetic moments are selected randomly to be half up and half down for {B} site elements. The electronic and atomic relaxation convergence criteria were 8×10^{-5} and 0.04 eV Å^{-1}, respectively. These settings

provide a reasonable compromise between accuracy and efficiency for a large number of MC trial calculations.

A descriptor called bond valence sum (BVS) developed by Brown and Shannon was adopted to analyze the relation between bond strength and bond length.[55] Note that the BVS values of the single components from the DFT calculation are consistently lower than the experimental BVS due to the GGA + U method underbinding the structure.[55,56] We focused on the comparison of DFT-computed bond valence sum (BVS) between the single components ($SrMnO_3$, $LaFeO_3$, $LaCoO_3$, and $LaAlO_3$) and $(La_{0.75}Sr_{0.25})$-$(Mn_{0.25}Fe_{0.25}Co_{0.25}Al_{0.25})O_3$ under the similar calculation conditions. The expression for a B element's bond valence sum is defined as follows:

$$V = \sum_i \exp\left(\frac{R_0 - R_i}{b}\right) \tag{1}$$

where R_0 and b are tabulated parameters from experiments (Table S4), R_i is the corresponding B−O bond length, and the sum goes over all six B−O bonds for a B centered octahedron. The bond valence theory predicts an outcome that is close to the oxidation state.

Local bond distortion occurs in compositional complex materials, and it can be measured by a discrepancy factor d:[56]

$$d_i = V_i - Z_i \tag{2}$$

where V_i is the BVS value for ion i and Z_i is the oxidation number for ion i (positive for a cation, negative for an anion). A positive d_i represents a compression of ion surrounding bonds, while a negative one stands for stretching. Furthermore, the global instability index
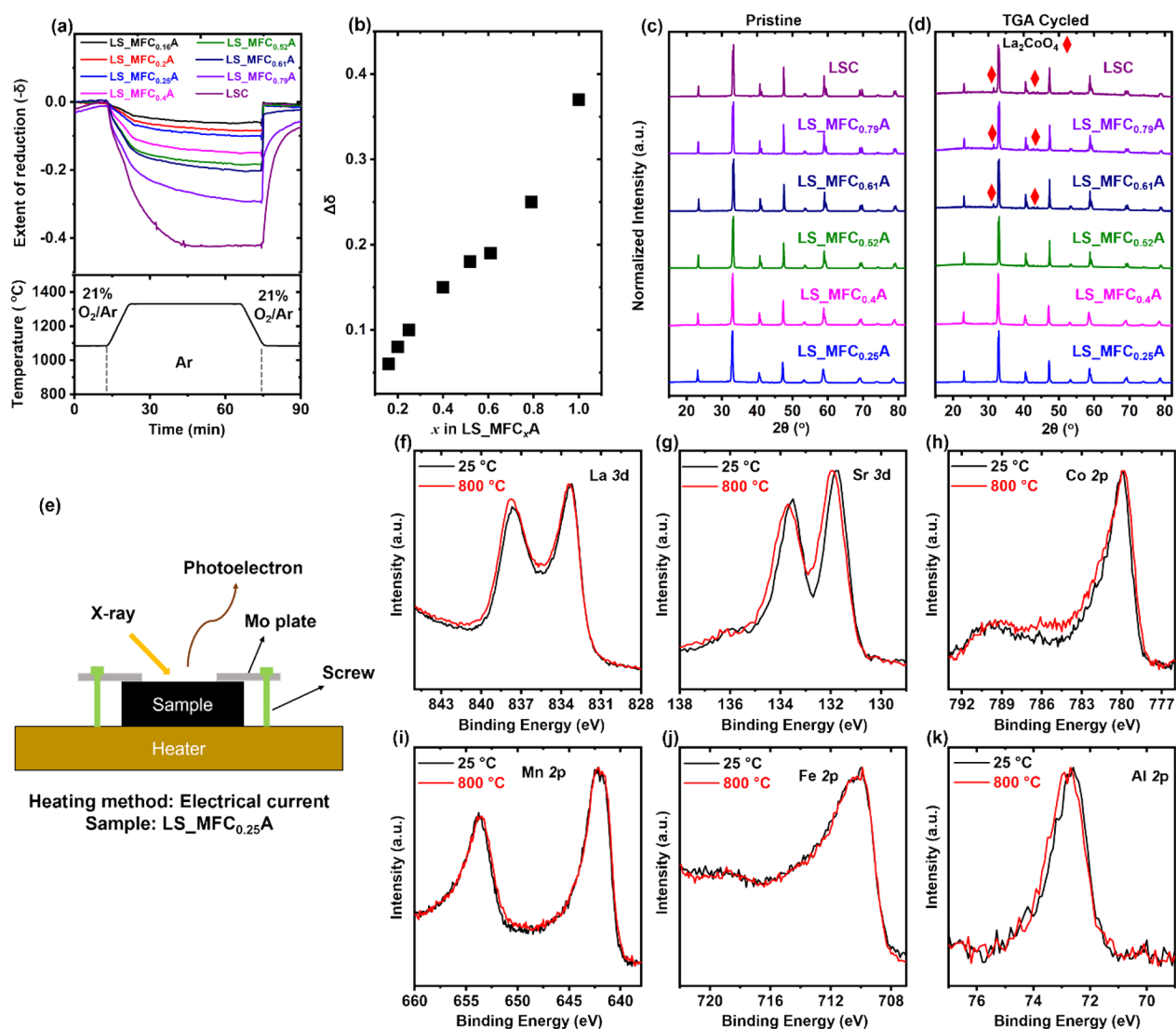
Figure 2. (a) TGA tests of LS_MFC$_x$A with x ranging from 0.16 to 1 to evaluate the extent of reduction (formation of oxygen vacancies) at 1350 °C for 45 min in Ar and reoxidation at 1100 °C in 21% O$_2$ balanced with Ar. (b) Correlation of $\Delta\delta$ with x in LS_MFC$_x$A. Comparison of XRD patterns (c) before and (d) after TGA experiments. A La$_2$CoO$_4$ secondary phase formed in LS_MFC$_x$A ($x \geq 0.61$). (e) Schematic of the in situ XPS setup and the normalized (f) La 3d, (g) Sr 3d, (h) Co 2p, (i) Mn 2p, (j) Fe 2p, and (k) Al 2p peaks of LS_MFC$_{0.25}$A at 25 and 800 °C.

G,[56] the root-mean-square value of the discrepancy factors over the whole system that quantifies the strain experienced by the structure as a whole, is defined as follows:

$$G = \left(\sum_i d_i^2 / N \right)^{1/2}$$

(3)

Additional experimental details of material characterization and kinetic properties and analyses can be found in the Supporting Information.

3. RESULTS AND DISCUSSION

Table 1 shows the sample abbreviations and nominal compositions for this LS_MFC$_x$A series of CCPOs. The XRD pattern (Figure 1a) reveals that LS_MFC$_x$A adopted a rhombohedral structure ($R\bar{3}c$), with the peak splitting at 2θ of 32.8° (Figure 1b). Rietveld refinements confirm the $R\bar{3}c$ phase for all compositions by assuming random B site occupation of Mn, Fe, Co, and Al (Figure S2 and Table S1). As the Co content increases in LS_MFC$_x$A, the diffraction peaks gradually shift to a higher 2θ angle, indicating a decrease in

lattice parameters, which is ascribed to the smaller ionic radius of Co^{3+} (0.545 Å) compared to an average ionic radius of other B-site elements (0.553 Å).[21,57] The apparent peak splitting with an increased Co amount in Figure 1b may be due to sharper XRD peaks (presumably related to more coarsening with increasing Co content). This is more clearly evident in Figure S2. To probe the phase stability of LS_MFC$_x$A under thermally reducing environments, LS_MFC$_{0.16}$A was selected to perform HT-XRD. Figure 1c displays that LS_MFC$_{0.16}$A showed phase stability at 1350 °C and maintained the $R\bar{3}c$ rhombohedral structure without phase transition under the reducing conditions, except for the slight peak shifts (lattice expansion) due to the thermal expansion and oxygen loss.[58−60] After the O$_2$ uptake at 800 °C, the lattice recovered to the initial state. Typical HT-XRD patterns were refined (Figures S3 and S4), showing that the crystallographic structure was maintained during the thermal reduction and oxidation conditions. The atomic structure and elemental distribution of LS_MFC$_{0.25}$A were characterized by scanning transmission electron microscopy (STEM) high-angle annular dark field
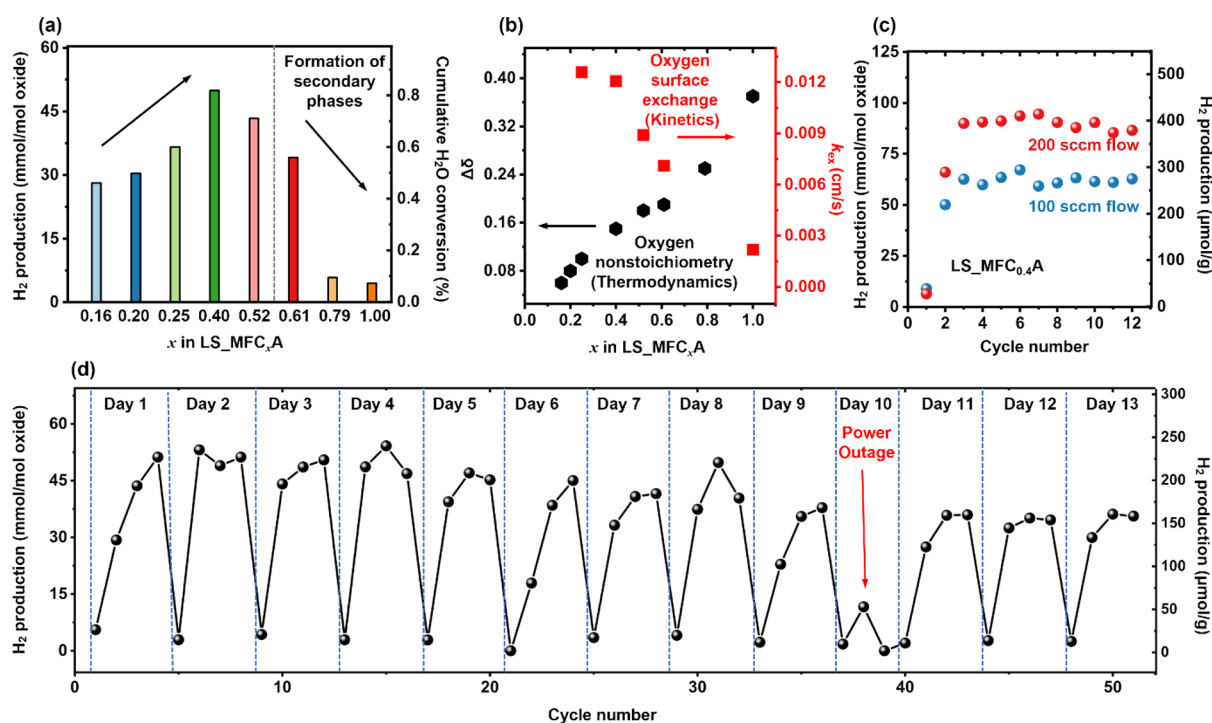
Figure 3. (a) Average hydrogen production and cumulative H_2O conversion extent of two stabilized cycles for LS_MFC$_x$A. The reduction was conducted at 1350 °C (T_{Re}) in N_2 for 45 min and oxidation was performed at 1100 °C (T_{Ox}) in 40 vol % H_2O for 15 min with a gas flow rate of 100 sccm. H_2 production shows a volcano plot shape with respect to the Co molar ratio in LS_MFC$_x$A. (b) Dependences of $\Delta\delta$ (measured by TGA) and oxygen surface exchange coefficient k_{ex} (measured by electrical conductivity relaxation) on the Co content in LS_MFC$_x$A. The thermodynamic ($\Delta\delta$) and kinetic (k_{ex}) properties demonstrate opposite correlation with the Co molar ratio in LS_MFC$_x$A. (c) $\overline{H_2}$ production stability of LS_MFC$_{0.4}$A under different flow rates during the uninterrupted cycling (T_{Re} = 1350 °C for 30 min in N_2 and T_{Ox} = 1100 °C for 30 min in 40 vol % steam). (d) Long-term STCH cycling of LS_MFC$_{0.4}$A under harsh interrupted cycling conditions involving startup heating and shutdown cooling at a STCH condition producing significant (but not maximized) H_2 production. Specifically, the sample was heated in the morning and cooled down to room temperature at night and four cycles were performed per day (using the STCH condition: T_{Re} = 1350 °C for 45 min in N_2 and T_{Ox} = 1100 °C for 15 min in 40 vol % steam with a gas flow rate of 100 sccm). This simulates the real day–night cycle conditions for STCH rather than uninterrupted cycling. Background H_2 production from catalytic water thermolysis was subtracted from the total H_2 production, and only the H_2 production from the redox reaction was illustrated.

(HAADF) imaging with energy-dispersive spectroscopy (EDS) (Figure 1d), which suggested a homogeneous elemental distribution of cation elements. The XRD and EDS mapping results indicate a long-range random B site occupation. The schematic structure is shown in Figure 1e.

To quantify the redox capability, LS_MFC$_x$A samples were tested by TGA.[61] The reversible extent of reduction ($\Delta\delta$) displays a decreasing trend with narrower temperature swing (Figure S5). The reduction reaction is endothermic, which is thermodynamically favored at a high temperature, while the oxidation reaction is exothermic that is thermodynamically favored at a low temperature (but it may be not kinetically favored at a very low temperature). Therefore, a wider temperature swing is a favorable driving force to enhance the reversible $\Delta\delta$. The TGA experiments (Figure 2a) show that $\Delta\delta$ monotonically increases with the molar fraction of Co in the B site of LS_MFC$_x$A (Figure 2b). The endmember of simple perovskite LSC can greatly be reduced with $\Delta\delta$ = 0.37 compared to LS_MFC$_{0.16}$A with the smallest $\Delta\delta$ = 0.06. When $x \leq 0.52$, the reduced samples were fully reoxidized under a 21% O_2 environment in 1–2 s. In contrast, when x was increased beyond ~0.61, the samples underwent a sluggish reoxidation process and could not be recovered to a full oxidation state within 25 min under 21% O_2. The low reoxidation rate under a high P_{O_2} of 21% indicates that the driving force for reoxidation can be a limited factor for these

compositions (LS_MFC$_x$A, $x \geq 0.61$). Moreover, the incomplete reoxidation process observed in LS_MFC$_x$A ($x \geq 0.61$) also implies a potential irreversible phase transformation or secondary phase precipitation during the redox cycling. The XRD patterns for LS_MFC$_x$A before and after the TGA measurements were compared (Figure 2c,d). A Co-enriched Ruddlesden−Popper (RP) La$_2$CoO$_4$ secondary phase was formed in LS_MFC$_{0.61}$A, LS_MFC$_{0.79}$A, and LSC, consistent with the reported poor phase stability of La$_{1-x}$Sr$_x$CoO$_3$.[26,27,29,30] In addition, many other perovskite oxides have been reported to demonstrate phase transformation and even serious decomposition after a thermochemical redox process, including BaCe$_{0.25}$Mn$_{0.75}$O$_3$,[24,30,34] Gd$_{0.5}$La$_{0.5}$Co$_{0.5}$Fe$_{0.5}$O$_3$,[25] La$_{0.8}$Sr$_{0.2}$MeO$_3$ (Me = Co, Ni, and Cu),[28] La$_{0.6}$Ca$_{0.4}$CoO$_3$,[31] Y$_{0.8}$Sr$_{0.2}$Mn$_{0.6}$Al$_{0.4}$O$_3$ and Y$_{0.8}$Sr$_{0.2}$MnO$_3$,[33] LaGa$_{1-y}$Co$_y$O$_{3-\delta}$ ($y \geq 0.1$) and La$_{1-x}$Sr$_x$Ga$_{0.5}$Co$_{0.5}$O$_{3-\delta}$ ($x = 0-0.5$).[21] In contrast, LS_MFC$_x$A ($x \leq 0.52$) showed no detectable secondary phase in the XRD patterns and displayed rapid and complete reoxidation. Therefore, the phase stability and redox reversibility of LS_MFC$_x$A ($x \leq 0.52$) make them suitable for STCH. Besides Co, we also tuned other B-site elements deviating from the equimolar composition or varied the fractions of Mn, Fe, and Al but fixing the Co fraction and measured their TGA results (Figure S6), which suggested that the Co content demon-

strated the most significant influence on the extent of reduction compared to other B-site elements.

To further confirm the redox sequence of B-site elements in LS_MFC_xA, in situ XPS was conducted to study the redox behavior of all cations by heating $LS\_MFC_{0.25}A$ to 800 °C (XPS heating limit) under vacuum (Figure 2e). The high-resolution XPS spectra of all cations at 25 and 800 °C are shown in Figure 2f−k. $LS\_MFC_{0.25}A$ showed a measurable $\Delta\delta$ of 0.03 at 800 °C (Figure S7). For the A-site elements, the left peak area of La $3d_{5/2}$ slightly increased, indicating pyrolysis of the surface-absorbed $La(OH)_3$ species at 800 °C. Sr also exhibited a side peak evolution, which was assigned to a slight Sr segregation that is widely found in solid oxide fuel cells.[62−64] For the B-site elements, Mn, Fe, and Co can be potentially redox-active. Al 2p showed negligible shift due to the stable Al^{3+} valence state. Co 2p showed an increased intensity and broadening of the side peak located at 787 eV, which is a Co^{2+} $2p_{3/2}$ satellite peak. This satellite peak evolution suggests that Co^{3+} is reduced to Co^{2+} during the in situ heating process, in agreement with previous reports.[65−67] In contrast, Fe 2p and Mn 2p had negligible changes upon heating. Meanwhile, the ex situ STEM electron energy loss spectroscopy (EELS) of $LS\_MFC_{0.4}A$ demonstrates that only Co has an obvious valence change (Figure S8). Therefore, Co is likely the primary redox element, consistent with the correlation between $\Delta\delta$ and Co content in TGA.

It is worth noting that the water thermolysis catalyzed by the alumina tube and samples could take place at 1100 °C in 40 vol % steam flow producing a small quantity of H_2, which has been recently reported.[68−70] Thus, the H_2 production from direct catalytic water splitting was measured (Figure S9) and subtracted from the total H_2 production to extract the true H_2 production from the redox reaction. Figure 3a shows the molar H_2 production per mole of various LS_MFC_xA under the given conditions (Figure S10 displaying molar H_2 production per gram of LS_MFC_xA). The hydrogen production increased from $LS\_MFC_{0.16}A$ to $LS\_MFC_{0.4}A$ and then rapidly fell after $x = 0.61$. The relationship of H_2 production with the Co content has a volcano shape with the peak H_2 production achieved by $LS\_MFC_{0.4}A$, similar to the observed trend in $La(Ga_{1−y}Co_y)O_3$.[21] Under this condition, $LS\_MFC_{0.4}A$ produced the highest H_2 production (49.88 mmol $mol_{oxide}^{−1}$), although it had a medium $\Delta\delta$. In contrast, the simple perovskite LSC showed a minimal H_2 production (4.48 mmol $mol_{oxide}^{−1}$) despite its largest $\Delta\delta$. The hydrogen production is also listed in Table S2. The molar ratio of H_2 to O_2 produced in the oxidation and reduction steps, respectively, is 2:1 (Figure S11), suggesting that water splitting is realized by the redox reaction.

The volcano-shaped plot of hydrogen production vs Co molar ratio may be related to the trade-off between the thermodynamic and kinetic properties, as shown in Figure 3b. The intrinsic kinetic properties of the LS_MFC_xA series were examined by an electrical conductivity relaxation (ECR) technique, which can quantify the oxygen surface reaction coefficient k_{ex}, i.e., the proportionality between the rate of oxygen incorporation and deviation of surface oxygen concentration by monitoring the response of electrical conductivity to the change of P_{O_2}.[71,72] It is found that the thermodynamic and kinetic properties can be readily tailored by tuning the Co content in LS_MFC_xA. Figure 3b illustrates an opposite correlation of the thermodynamic ($\Delta\delta$) and

kinetics (k_{ex}) properties with the Co content, where more Co decreases the kinetics but increases $\Delta\delta$. In this series, $LS\_MFC_{0.4}A$ likely achieved a balance between the thermodynamic and kinetic properties, delivering the highest H_2 production within the given duration. The oxygen uptake and release tests further confirm the superior oxygen incorporating kinetics of LS_MFC_xA with a lower Co content (Figure S12). Additionally, LS_MFC_xA with a high Co content ($x > 0.52$) showed inferior phase stability, where the formation of the secondary RP phase (Figure 2c,d) is unfavorable for the H_2 production. Therefore, we focused on the optimal composition $LS\_MFC_{0.4}A$ to further investigate its STCH performance.

The hydrogen production is influenced by the testing conditions, such as the gas flow rate, reaction temperature (T_{Re} and T_{Ox}), and reaction time (t_{Re} and t_{Ox}). Therefore, the effects of these factors on the H_2 production of $LS\_MFC_{0.4}A$ were systematically investigated. The reduction temperature was fixed at 1350 °C. Table 2 summarizes the cumulative H_2 production in the stabilized cycle under different conditions. A larger temperature swing by reducing the oxidation temperature (C1, C2, and C3) reduced the H_2 production in a 1 h cycle, although the larger temperature swing is supposed to thermodynamically favor the H_2 production. The elevated oxidation temperature (C3) rendered H_2 production four times higher than the lower oxidation temperature (C1) under the given reduction and oxidation durations and flow rate, as the former promoted the reaction kinetics. Therefore, the oxidative water splitting step ($ABO_{3−\delta} + \delta H_2O = ABO_3 + \delta H_2$) benefits from an increase in the oxidation temperature (C1 → C3), indicating that this H_2 production step is primarily limited by kinetics. A similar positive effect of elevated oxidation temperature on the H_2 production has been reported in $Sr(Ti_{0.5}Mn_{0.5})O_3$ and $Ca(Ti_{0.5}Mn_{0.5})O_3$.[19,49] Furthermore, when T_{Ox} was higher than 1200 °C, the alumina tube produced a substantial H_2 background level arising from its catalytic water thermolysis. Thus, we did not further investigate higher oxidation temperatures. The extended oxidation time enhanced the H_2 production, confirming the kinetically limited oxidative water splitting step. Increasing the flow rate of steam also boosted the H_2 production from 61.50 mmol $mol_{oxide}^{−1}$ at 100 sccm to 89.97 mmol $mol_{oxide}^{−1}$ at 200 sccm within 30 min oxidation time, likely due to the improved mass transfer of steam and rapid removal of the H_2 product. The oxidation reaction rate is limited by the supply of H_2O. The experimentally measured H_2 production (89.97 mmol $mol_{oxide}^{−1}$) is very close to the theoretically calculated thermodynamic limit value of 93.39 mmol $mol_{oxide}^{−1}$ (see next discussion). The highest H_2 production of 89.97 mmol $mol_{oxide}^{−1}$ in a short duration (30 min oxidation and 30 min reduction) for $LS\_MFC_{0.4}A$ is higher than those of reported STCH materials with longer oxidation and reduction durations (Table S3). For this fundamental research, we used an excess of steam feeding and a small quantity of perovskite oxide powder (∼0.1 g) to ensure the sufficient steam/solid contact and mass transfer for measurement of the thermodynamic limit of H_2 production to analyze the correlation of H_2 production with material properties. Therefore, a large excess of steam feedstock makes the cumulative H_2O conversion extent less than 1% as shown in Figure 3a and Table 2. For future engineering design and evaluation of its viability for practical application, the steam reactant feeding should be limited, and a large size of reticulated porous ceramic monolith should be

used for improving the conversion extents to an industrially meaningful steam-to-H_2 conversion.[73]

We investigated the cyclability of LS_MFC$_{0.4}$A under both uninterrupted and harsher interrupted conditions. Figure 3c exhibits the uninterrupted cycling test results. After the initial two activation cycles, LS_MFC$_{0.4}$A maintained stable H_2 productions of 61.50 mmol mol^{-1} (270 ± 9 μmol g^{-1}) and 89.97 mmol mol^{-1} (395 ± 11 μmol g^{-1}) at steam flow rates of 100 and 200 sccm for the following 10 consecutive cycles, respectively. The STCH cycling stability of LS_MFC$_{0.4}$A under the continuous testing conditions is comparable to those of reported STCH redox oxides, whereas the stable H_2 production of LS_MFC$_{0.4}$A is higher (Table S3). The particle morphology and EDS mapping of pristine and cycled LS_MFC$_{0.4}$A are shown in Figure S13. LS_MFC$_{0.4}$A after 12 cycles did not show significant element segregation despite apparent sintered particles. Note that the seemingly inhomogeneity in EDS maps of some elements such as Sr and Al compared to other elements is owing to the different element interaction volume rather than their inhomogeneous distribution. In general, the configurational entropy of a multicomponent solid solution can be enhanced by mixing a large number of cations ideally in equiatomic proportions and a single solid-solution phase can be stabilized if the entropy contribution overcomes the enthalpy-driven phase separation.[35,74,75] Therefore, the phase stability of CCPO after redox cycling is possibly attributed to the entropy stabilization effect, stabilizing a single solid-solution phase and inhibiting precipitation during the thermal or electrochemical redox cycling.[76−80] For the practical STCH applications, the diurnal cycle of sunlight irradiation should be considered without the viable, efficient, large-scale, and stable thermal energy storage technology[81−83] as the STCH materials may subject to drastic temperature swing between elevated temperatures under an 8 h strong sunlight irradiation (operation mode) in the day and low temperatures of long-time cooling stage (downtime mode) in the night. In stark contrast to the ideal uninterrupted cycling condition using a stable heat source, such interrupted cycling involving startup heating and shutdown cooling is a harsh condition to the STCH application, which can induce thermal fatigue, impair the structural integrity, and dramatically deteriorate the H_2 production cycle.[84,85] A similar challenge exists in other solar-driven hydrogen production technologies such as photovoltaic-driven water electrolysis, where the startup and shutdown cycling due to the day−night cycle causes degradation of electrocatalysts.[86−89] Therefore, the interrupted cycling stability of LS_MFC$_{0.4}$A for thermochemical hydrogen production was evaluated under the daily startup and shutdown cycling for 13 days (51 cycles) to simulate the real diurnal cycle. Note that more cycles per day may be carried out in a real reactor with faster ramping rates, in comparison with our homemade testing reactor. Figure 3d demonstrates that LS_MFC$_{0.4}$A showed around 30% decay in H_2 production under this harsh condition after 13 days, indicating that its moderate cycling stability against thermal fatigue and redox degradation requires further improvement for practical application. To the best of our knowledge, few research on development of STCH materials has paid attention to the cyclability under this harsh condition. However, the stability of a Cu-ZnO-Al$_2$O$_3$ catalyst for simulated solar methanol production has been investigated under the daily startup−shutdown conditions, showing 27% activity degradation during 27 cycles (6.3 h operation and 17.7 h shutdown per cycle).[84] Future efforts are needed to enhance the cycling stability of thermochemical redox oxides under the interrupted conditions for real-world applications. The SEM images and EDS mapping (Figure S13c) of LS_MFC$_{0.4}$A after 51 cycles displayed sintered morphology but homogeneous elemental distribution.

In addition to the proven excellent thermal stability and intrinsic surface oxygen exchange kinetics, two thermodynamic properties, enthalpy and entropy of reduction, are important factors determining the performance of STCH materials.[51,90,91] Therefore, we carried out the measurements of the oxygen non-stoichiometry over a range of temperatures and P_{O_2} values for LS_MFC$_{0.4}$A using a widely reported TGA protocol (see details in Figure S14).[19,49,92−94] Figure 4a shows the oxygen
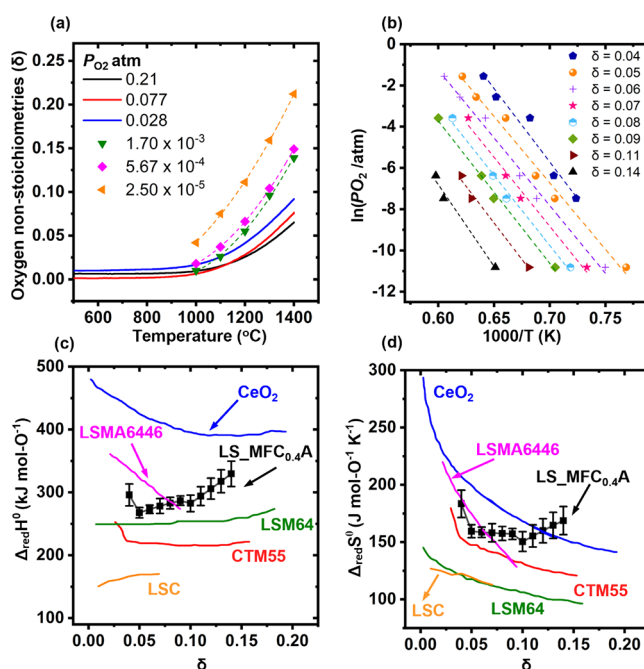

Figure 4. (a) Oxygen non-stoichiometry of LS_MFC$_{0.4}$A as a function of temperature as measured by continuous (solid lines) and stepwise (symbols) heating under the given P_{O_2} values. (b) Arrhenius representation of $\ln(P_{O_2})$ vs $1000/T$ for extraction of thermodynamic properties (e.g., enthalpy and entropy of reduction) by the van't Hoff method at typical fixed δ values as indicated. Symbols and dashed lines in the profile represent the measured and linearly fitted results, respectively. (c) Standard enthalpy and (d) entropy of reduction calculated for LS_MFC$_{0.4}$A and comparison to those of some reported STCH and redox oxide materials. The error bars of LS_MFC$_{0.4}$A came from the error of its linear fitting. Data for CeO$_2$,[96] La$_{0.6}$Sr$_{0.4}$Mn$_{0.4}$Al$_{0.6}$O$_3$ (LSMA6446),[97] cubic CaMn$_{0.5}$Ti$_{0.5}$O$_3$ (CTM55),[19] La$_{0.6}$Sr$_{0.4}$MnO$_3$ (LSM64),[98] and La$_{0.8}$Sr$_{0.2}$CoO$_3$ (LSC)[93] are replotted from prior studies cited herein.

non-stoichiometry of LS_MFC$_{0.4}$A as a function of temperature measured by continuous ($P_{O_2} \geq 0.028$ atm) and stepwise ($P_{O_2} \leq 1.7 \times 10^{-3}$ atm) heating under the given P_{O_2} values. Following the van't Hoff method,[19,95,96] the enthalpy and entropy of reduction can be correlated with temperature and P_{O_2} according to the following equation:

$$R \ln(P_{O_2})^{1/2} = -\frac{\Delta_{red}H(\delta)}{T} + \Delta_{red}S(\delta) \tag{4}$$
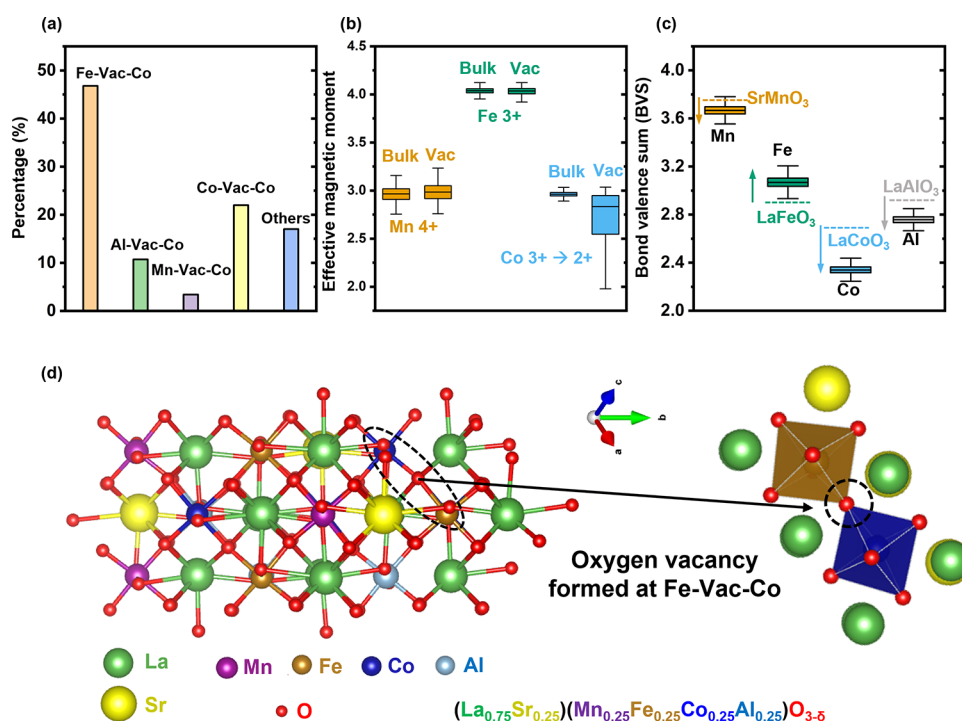
Figure 5. (a) Vacancy (Vac) B-site first nearest neighbor (FNN) distributions show dominant Co preference over other B-site elements. (b) Local magnetic moment evolution between bulk and vacancy configurations for 3d orbitals of Mn, Fe, and Co from saved bulk structures (∼2600 configurations) and vacancy structures (∼3000 configurations) shows that Co goes through the largest magnitude change when a single neutral oxygen vacancy is formed. The bulk structure represents the supercell structure before introducing an oxygen vacancy. (c) Calculated bond valence sum (BVS) for Mn, Fe, Co, and Al octahedra in the $(La_{0.75}Sr_{0.25})(Mn_{0.25}Fe_{0.25}Co_{0.25}Al_{0.25})O_3$ structure (solid lines for median BVS values and box plots). The dashed lines present the BVS values of $SrMnO_3$, $LaFeO_3$, $LaCoO_3$, and $LaAlO_3$ simple perovskite references based on our DFT calculations. (d) Representative of the simulation cell containing oxygen vacancy with Fe and Co as FNN of the position with the largest percentage where an oxygen vacancy is formed.

where R is the universal gas constant and P_{O_2} is equal to the oxygen partial pressure referenced to the standard gas pressure (1 atm). T is the temperature in Kelvin. $\Delta_{red}H(\delta)$ and $\Delta_{red}S(\delta)$ are the standard enthalpy and entropy of reduction, respectively, which are dependent on δ and defined on a per mole of oxygen basis but have negligible dependence on temperature.

An Arrhenius plot of $\ln(P_{O_2})$ vs $1000/T$ at each specified δ value with linear fitting can be obtained (Figure 4b), from which $\Delta_{red}H(\delta)$ and $\Delta_{red}S(\delta)$ can be extracted from the slope and intercept, respectively. In this way, the enthalpy and entropy of $LS\_MFC_{0.4}A$ as a function of δ are obtained (Figure 4c,d) and compared with those of some reported STCH and redox oxide materials such as CeO_2,[96] cubic $Ca(Mn_{0.5}Ti_{0.5})$-$O_{3-\delta}$ (CTM55),[19] $La_{0.6}Sr_{0.4}MnO_{3-\delta}$ (LSM64),[98] $La_{0.6}Sr_{0.4}Mn_{0.4}Al_{0.6}O_{3-\delta}$ (LSMA6446),[97] and $La_{0.8}Sr_{0.2}CoO_3$ (LSC).[93]

Previous experimental and theoretical studies suggested that a combination of intermediate enthalpy and large entropy is favorable for STCH from water splitting.[19,94,97,99] For perovskite materials, the enthalpy of reduction can be tuned by the dopants[100] and is desirably constrained to a certain moderate range (neither too high nor too low), which may follow a Sabatier principle. A low enthalpy of reduction usually accompanies a low entropy of reduction under the given conditions (temperature and P_{O_2}) for a variety of redox oxide materials, rendering favorable reduction reactions but not oxidative water splitting.[99,101] In contrast, a high enthalpy of reduction enables a high energy penalty for thermal reduction.

$LS\_MFC_{0.4}A$ shows enthalpy and entropy values comparable to LSMA6446 and CTM55, which have been identified to have prominent hydrogen production with an appropriate combination of moderate enthalpy and relatively large entropy.[19,97] With the measured thermodynamic properties, the equilibrium H_2 production was calculated to be 93.39 mmol mol_{oxide}^{-1} under the condition C6 listed in Table 2. Compared with ceria, $LS\_MFC_{0.4}A$ possesses a much lower enthalpy but similar entropy of reduction when $\Delta\delta$ is more than 0.1, suggesting its potential for high H_2 production under a lower reduction temperature. As shown in the TGA results (Figure 2), the $\Delta\delta$ value of LS_MFC_xA increases with x, possibly due to the decreased enthalpy of reduction upon the increasing content of Co. For example, the LSC material shows a small enthalpy (<200 kJ mol^{-1}) and entropy simultaneously, suggesting that it tends to have a large $\Delta\delta$ but poor oxidative water splitting capability. This is in good agreement with our TGA and STCH results of LSC. $LS\_MFC_{0.4}A$ displays the highest hydrogen production in this LS_MFC_xA series. This finding suggests that while maintaining a moderate enthalpy of reduction, multiple cations in LS_MFC_xA may introduce extra configurational entropy to fulfill the needs of oxygen vacancy formation and electronic and ionic configurational entropy change.[102,103]

To elucidate why Co is the most redox active in LS_MFC_xA and shed light on the factors governing the priority of redox behavior, we employed MC sampling based on DFT. It was found that $Pnma$, $R\bar{3}c$, and $Pm\bar{3}m$ structures have similar energies and configurations. Thus, only $R\bar{3}c$ results were reported here, consistent with the XRD patterns of LS_MFC_xA. For bulk structures without oxygen vacancies,

the nearest neighbor check was adopted to confirm if there are any B-cations' configurational preferences. The oxygen atom is surrounded by four first nearest neighbors (FNN) with two A-site atoms and two B-site atoms in the $R\bar{3}c$ structure. In the accepted low energy $(La_{0.75}Sr_{0.25})(Mn_{0.25}Fe_{0.25}Co_{0.25}Al_{0.25})O_3$ 80-atom supercell, the probability of finding oxygen FNN B-site elements to be the same type of B_1 element is $P(B_1 - O - B_1) = \frac{4}{16} \times \frac{3}{15} = 0.05$. The probability to find two atoms of different elements $B_1 - B_2$ is $P(B_1 - O - B_2) = 2 \times \frac{4}{16} \times \frac{4}{15} = \frac{2}{15} \approx 0.133$, suggesting no configurational preference for B-site cation combinations. Therefore, the cation configuration of the fully oxidized bulk structure is similar to a random distribution without signatures of B-site short-range ordering consistent with the defined CCPO structure. By introducing a single neutral oxygen vacancy, the configurational preference is changed. For the accepted vacancy containing configurations, the B-site distribution in Figure 5a shows that 83% of the combinations (incl. Fe-Vac-Co (46.8%), Al-Vac-Co (10.7%), Mn-Vac-Co (3.4%), and Co-Vac-Co (22.1%)) prefer to have at least one Co at its FNN position in the $R\bar{3}c$ structure, strongly deviating from the probability in a random distribution ($0.05 + 0.133 \times 3 = 44.9\%$). The possible positions of formed oxygen vacancy are illustrated in Figure 5d (Fe-Vac-Co) and Figures S15−S21. Therefore, the computed probability of the oxygen FNN {B} site strongly deviates from the probability in a random oxygen FNN {B} site distribution (83% versus 44.9%) for at least one Co in the B site, suggesting the Co preference in vacancy configurations. A further analysis of the effective magnetic moments (unpair electrons) of the B-site transition metal elements excluding the non-magnetic Al in the accepted bulk and vacancy systems was conducted to reveal how the oxygen vacancy changes the cation valence states. The magnetic moment magnitude is directly correlated with the oxidation state of the magnetic transition metal. The statistical distribution plotted in Figure 5b shows the respective magnetic moment magnitude changes of Mn, Fe, and Co in bulk and vacancy configurations. Before the vacancy is formed (i.e., bulk), the median magnetic moment magnitudes for Mn, Fe, and Co are 3.0, 4.0, and 2.9, corresponding to oxidation states of Mn^{4+}, Fe^{3+}, and high spin Co^{3+}, respectively. After introducing a single oxygen vacancy, Co is the element that has the greatest magnetic moment magnitude change ($Co^{3+} \rightarrow Co^{2+}$) and broadest distribution. The magnetic moment distribution of Mn is slightly broadened. The magnetic moment distribution of Fe is almost unchanged. Therefore, the Co^{3+}/Co^{2+} redox pair is the most active in response to the formation of oxygen vacancies in the LS_MFC_xA systems, possibly followed by Mn^{4+}/Mn^{3+}.

A possible reason for the Co preference in vacancy configurations is the Co−O bond stretching effect. Since neutral vacancy formation causes volume expansion in many oxides, a tensile stress (bond stretching) in the bulk will lower the vacancy formation energy.[104−106] In the CCPOs, local bond stretching may create more space to favor oxygen vacancy formation. To capture the local bond strength, the bond valence sum (BVS) descriptor was analyzed.[55] The BVS for each B-site cation in a perfect structure is close to its oxidation number. A lower (higher) value is considered as an elongated (compressed) bond with weaker (stronger) bond strength. For example, using the tabulated parameters (Table S4) developed by fitting experiments,[107] the BVS for Mn^{4+} in

$SrMnO_3$, Fe^{3+} in $LaFeO_3$, and Co^{3+} in $LaCoO_3$, and Al^{3+} in $LaAlO_3$ (dashed lines in Figure 5c) are very close to 4.0, 3.0, 2.9, and 3.0 for their experimentally reported structures, respectively. The DFT-calculated BVS of ternary perovskites (e.g., $SrMnO_3$, $LaFeO_3$, $LaCoO_3$, and $LaAlO_3$) serves as the references to compare with that of the bulk $(La_{0.75}Sr_{0.25})$-$(Mn_{0.25}Fe_{0.25}Co_{0.25}Al_{0.25})O_3$ (solid lines and box plots in Figure 5c). The distribution of BVS for Co in $(La_{0.75}Sr_{0.25})$-$(Mn_{0.25}Fe_{0.25}Co_{0.25}Al_{0.25})O_3$ is greatly lowered compared to that in the DFT reference structure ($LaCoO_3$), indicating a distortion-induced bond elongation and weakening effect. The distributions of BVS for Mn and Al in $(La_{0.75}Sr_{0.25})$-$(Mn_{0.25}Fe_{0.25}Co_{0.25}Al_{0.25})O_3$ are slightly lower than those in their DFT-relaxed ternary perovskite references, while the BVS for Fe in $(La_{0.75}Sr_{0.25})(Mn_{0.25}Fe_{0.25}Co_{0.25}Al_{0.25})O_3$ is increased compared to that in the $LaFeO_3$ reference. These results demonstrate a greatly weakened Co−O bond, slightly weakened Mn−O and Al−O bonds, and strengthened Fe−O bonds in CCPO.

We further evaluated the deviation of BVS on each cation in $(La_{0.75}Sr_{0.25})(Mn_{0.25}Fe_{0.25}Co_{0.25}Al_{0.25})O_3$ from its oxidation number, and the root-mean-square value of this deviation for all the cations, i.e., the global stability index G. All Sr and Fe ions are under compression, and all La, Mn, Co, and Al are under tension, while Co shows the largest negative deviation from its perfect BVS. The calculated global instability index G for saved bulk structures ranges from 0.217 to 0.233 vu, indicating strained structures. Hence, we propose that the Co preference in vacancy configurations is due to the Co−O bond stretching effect. Although Mn^{4+} may be more reducible than Co^{3+} based on the classical charges, the Co−O bond stretching outweighs the tendency to generate vacancies near Mn^{4+}, resulting in the tendency to form oxygen vacancies adjacent to Co at its FNN position.

4. CONCLUSIONS

In this study, we demonstrated a new class of medium- to high-entropy CCPOs, LS_MFC_xA, with tunable thermodynamic and kinetics properties for two-step thermochemical water splitting. The reversible extent of reduction ($\Delta\delta$) increases with the rising Co content (x), whereas the intrinsic kinetics (oxygen surface exchange coefficient) shows a decreased trend with the increasing x. $LS\_MFC_{0.4}A$ $((La_{0.8}Sr_{0.2})$-$(Mn_{0.2}Fe_{0.2}Co_{0.4}Al_{0.2})O_3)$ exhibits an optimal balance between intrinsic thermodynamics and kinetics as well as exceptional phase stability during the redox cycling and a favorable combination of moderate reduction enthalpy (268−329 kJ $(mol\text{-}O)^{-1}$) and high entropy (150−180 J $(mol\text{-}O)^{-1}$ K^{-1}). These merits of $LS\_MFC_{0.4}A$ enable a maximum hydrogen production of 89.97 mmol mol_{oxide}^{-1} within a short 1 h duration (30 min reduction and 30 min oxidation) under optimized STCH conditions as well as fair STCH cycling durability. The preferred redox of Co over other B-site metals is revealed by the TGA and in situ XPS. A combined MC-DFT computation demonstrates that an oxygen vacancy prefers to form in the vicinity of the position with at least one Co at its first nearest neighbor. Analysis of the magnetic moments of the B-site metals confirms that the Co redox valence change is the most active in response to the formation of oxygen vacancies. The bond valence sum results demonstrate a greatly weakened Co−O bond, slightly weakened Mn−O and Al−O bonds, and strengthened Fe−O bonds. The Co−O bond stretching effect

rationalizes the dependence of $\Delta\delta$ on the Co content and its dominance in the redox behavior of LS_MFC$_x$A.

In general, we showed the importance of achieving a trade-off of thermodynamic and kinetic properties for optimized STCH performance. This study further exemplifies that non-equimolar compositions outperform their higher-entropy equimolar counterparts in this two-step STCH application. While an entropy effect may stabilize the phase, maximizing configurational entropy is not always needed ($S_{configuration}$ = 0.943k_B per B-site cation in equimolar LS_MFC$_{0.25}$A versus $S_{configuration}$ = 0.916k_B per B-site cation in non-equimolar LS_MFC$_{0.4}$A, where k_B is the Boltzmann constant). The non-equimolar compositional design of CCPOs provides a way to balance the thermodynamic and kinetic properties to achieve better STCH performance.

This work explores CCPOs with tunable redox, thermodynamic, and kinetic properties for STCH and thermochemical looping and a new computation paradigm to predict the redox behavior. Future efforts will be focused on investigating the mechanical strength and thermodynamic stability of porous ceramic monoliths during the thermochemical redox cycling process. Although kilowatt-level reactors for thermochemical production of solar fuels have recently been demonstrated,[7,108] various technical challenges still exist toward realization of the industrial STCH deployment in terms of the material and system scaling-up, reactant conversion extent, reaction selectivity, product purity, energy and power densities, energy efficiency, cycling stability under interrupted conditions, heat management, thermal energy storage, system complexity, and rigorous technoeconomic analysis, requiring continuous efforts of scientific and engineering communities. We believe that the emergent compositionally complex ceramics (CCCs),[45,46] including (but not limited to) high-entropy ceramics (HECs) as a subset, with tunable redox capability, thermodynamic, and kinetic properties and improved phase stability will be of broad interest to diverse applications such as thermochemical looping, heterogeneous catalysis, and electrochemical energy conversion and storage.

■ ASSOCIATED CONTENT

ⓢ Supporting Information

The Supporting Information is available free of charge at https://pubs.acs.org/doi/10.1021/acs.chemmater.2c03054.

> Additional details and information on material characterization and electrical conductivity relaxation; supplemental tables summarizing lattice parameters obtained by Rietveld refinements of XRD patterns, STCH production results, comparison of STCH production performances and BVS parameters; schematic of the homemade STCH reactor, Rietveld refinements of XRD and HT-XRD patterns, whole scan of HT-XRD, TGA results, STEM-EELS results, effect of direct catalytic water thermolysis in the STCH reactions, STCH production and cumulative H_2O conversion extent, MS results of STCH, SEM and EDS mapping, TGA results under different oxygen partial pressures, and various schematic structures of simulation cells containing oxygen vacancy with different B-site atoms as FNN (PDF)

■ AUTHOR INFORMATION

Corresponding Authors

Wei Li − *Department of Mechanical and Aerospace Engineering, Benjamin M. Statler College of Engineering and Mineral Resources, West Virginia University, Morgantown, West Virginia 26506, United States;* ⓞ orcid.org/0000-0003-2802-7443; Email: wei.li@mail.wvu.edu

Yue Qi − *School of Engineering, Brown University, Providence, Rhode Island 02912, United States;* Email: yueqi@brown.edu

Xingbo Liu − *Department of Mechanical and Aerospace Engineering, Benjamin M. Statler College of Engineering and Mineral Resources, West Virginia University, Morgantown, West Virginia 26506, United States;* ⓞ orcid.org/0000-0001-8720-7175; Email: xingbo.liu@mail.wvu.edu

Jian Luo − *Program of Materials Science and Engineering and Department of NanoEngineering, University of California San Diego, La Jolla, California 92093, United States;* ⓞ orcid.org/0000-0002-5424-0216; Email: jluo@alum.mit.edu

Authors

Dawei Zhang − *Program of Materials Science and Engineering, University of California San Diego, La Jolla, California 92093, United States*

Héctor A. De Santiago − *Department of Mechanical and Aerospace Engineering, Benjamin M. Statler College of Engineering and Mineral Resources, West Virginia University, Morgantown, West Virginia 26506, United States*

Boyuan Xu − *Department of Physics, Brown University, Providence, Rhode Island 02912, United States;* ⓞ orcid.org/0000-0002-7611-1706

Cijie Liu − *Department of Mechanical and Aerospace Engineering, Benjamin M. Statler College of Engineering and Mineral Resources, West Virginia University, Morgantown, West Virginia 26506, United States*

Jamie A. Trindell − *Sandia National Laboratories, Livermore, California 94551, United States;* ⓞ orcid.org/0000-0001-6453-021X

Jiyun Park − *School of Engineering, Brown University, Providence, Rhode Island 02912, United States*

Mark A. Rodriguez − *Sandia National Laboratories, Albuquerque, New Mexico 87185, United States*

Eric N. Coker − *Sandia National Laboratories, Albuquerque, New Mexico 87185, United States*

Joshua D. Sugar − *Sandia National Laboratories, Livermore, California 94551, United States*

Anthony H. McDaniel − *Sandia National Laboratories, Livermore, California 94551, United States*

Stephan Lany − *Materials Science Center, National Renewable Energy Laboratory, Golden, Colorado 80401, United States;* ⓞ orcid.org/0000-0002-8127-8885

Liang Ma − *Department of Mechanical and Aerospace Engineering, Benjamin M. Statler College of Engineering and Mineral Resources, West Virginia University, Morgantown, West Virginia 26506, United States; School of Materials Science and Engineering, Hebei University of Engineering, Handan, Hebei Province 056038, China*

Yi Wang − *Department of Mechanical and Aerospace Engineering, Benjamin M. Statler College of Engineering and Mineral Resources, West Virginia University, Morgantown, West Virginia 26506, United States*

Gregory Collins − *Department of Mechanical and Aerospace Engineering, Benjamin M. Statler College of Engineering and Mineral Resources, West Virginia University, Morgantown, West Virginia 26506, United States*

Hanchen Tian − *Department of Mechanical and Aerospace Engineering, Benjamin M. Statler College of Engineering and Mineral Resources, West Virginia University, Morgantown, West Virginia 26506, United States;* ● orcid.org/0000-0003-0044-5678

Wenyuan Li − *Department of Chemical and Biomedical Engineering, Benjamin M. Statler College of Engineering and Mineral Resources, West Virginia University, Morgantown, West Virginia 26506, United States;* ● orcid.org/0000-0002-8853-225X

Complete contact information is available at:
https://pubs.acs.org/10.1021/acs.chemmater.2c03054

Author Contributions

Notes

The authors declare no competing financial interest.

■ ACKNOWLEDGMENTS

■ REFERENCES

(1) Wee, J. H. Applications of Proton Exchange Membrane Fuel Cell Systems. *Renewable Sustainable Energy Rev.* **2007**, *11*, 1720−1738.

(2) Jiao, K.; Xuan, J.; Du, Q.; Bao, Z.; Xie, B.; Wang, B.; Zhao, Y.; Fan, L.; Wang, H.; Hou, Z.; Huo, S.; Brandon, N. P.; Yin, Y.; Guiver, M. D. Designing the next Generation of Proton-Exchange Membrane Fuel Cells. *Nature* **2021**, *595*, 361−369.

(3) Banham, D.; Kishimoto, T.; Zhou, Y.; Sato, T.; Bai, K.; Ozaki, J. I.; Imashiro, Y.; Ye, S. Critical Advancements in Achieving High Power and Stable Nonprecious Metal Catalyst-Based MEAs for Real-World Proton Exchange Membrane Fuel Cell Applications. *Sci. Adv.* **2018**, *4*, 7180.

(4) Ampelli, C.; Perathoner, S.; Centi, G. CO2 Utilization: An Enabling Element to Move to a Resource-and Energy-Efficient Chemical and Fuel Production. *Philos. Trans. R. Soc., A* **2015**, *373*, 20140177.

(5) Centi, G.; Quadrelli, E. A.; Perathoner, S. Catalysis for CO2 Conversion: A Key Technology for Rapid Introduction of Renewable Energy in the Value Chain of Chemical Industries. *Energy Environ. Sci.* **2013**, *6*, 1711−1731.

(6) Miller, J. E.; McDaniel, A. H.; Allendorf, M. D. Considerations in the Design of Materials for Solar-Driven Fuel Production Using Metal-Oxide Thermochemical Cycles. *Adv. Energy Mater.* **2014**, *4*, 1300469.

(7) Schäppi, R.; Rutz, D.; Dähler, F.; Muroyama, A.; Haueter, P.; Lilliestam, J.; Patt, A.; Furler, P.; Steinfeld, A. Drop-in Fuels from Sunlight and Air. *Nature* **2022**, *601*, 63−68.

(8) Steinfeld, A. Solar Thermochemical Production of Hydrogen - A Review. *Sol. Energy* **2005**, *78*, 603−615.

(9) Kodama, T.; Gokon, N. Thermochemical Cycles for High-Temperature Solar Hydrogen Production. *Chem. Rev.* **2007**, *107*, 4048−4077.

(10) Scheffe, J. R.; Steinfeld, A. Oxygen Exchange Materials for Solar Thermochemical Splitting of H2O and CO2: A Review. *Mater. Today* **2014**, *17*, 341−348.

(11) Bulfin, B.; Vieten, J.; Agrafiotis, C.; Roeb, M.; Sattler, C. Applications and Limitations of Two Step Metal Oxide Thermochemical Redox Cycles A Review. *J. Mater. Chem. A* **2017**, *5*, 18951−18966.

(12) Chueh, W. C.; Haile, S. M. Ceria as a Thermochemical Reaction Medium for Selectively Generating Syngas or Methane from H2O and CO2. *ChemSusChem* **2009**, *2*, 735−739.

(13) Chueh, W. C.; Falter, C.; Abbott, M.; Scipio, D.; Furler, P.; Haile, S. M.; Steinfeld, A. High-Flux Solar-Driven Thermochemical Dissociation of CO2 and H2O Using Nonstoichiometric Ceria. *Science* **2010**, *330*, 1797−1801.

(14) Muhich, C.; Steinfeld, A. Principles of Doping Ceria for the Solar Thermochemical Redox Splitting of H2O and CO2. *J. Mater. Chem. A* **2017**, *5*, 15578−15590.

(15) Oliveira, F. A. C.; Barreiros, M. A.; Haeussler, A.; Caetano, A. P. F.; Mouquinho, A. I.; e Silva, P. M. O.; Novais, R. M.; Pullar, R. C.; Stéphane, A. High Performance Cork-Templated Ceria for Solar Thermochemical Hydrogen Production via Two-Step Water-Splitting Cycles. *Sustainable Energy Fuels* **2020**, *4*, 3077−3089.

(16) Ermanoski, I.; Miller, J. E.; Allendorf, M. D. Efficiency Maximization in Solar-Thermochemical Fuel Production: Challenging the Concept of Isothermal Water Splitting. *Phys. Chem. Chem. Phys.* **2014**, *16*, 8418−8427.

(17) Emery, A. A.; Wolverton, C. High-Throughput DFT Calculations of Formation Energy, Stability and Oxygen Vacancy Formation Energy of ABO3 Perovskites. *Sci. Data* **2017**, *4*, 170153.

(18) Emery, A. A.; Saal, J. E.; Kirklin, S.; Hegde, V. I.; Wolverton, C. High-Throughput Computational Screening of Perovskites for Thermochemical Water Splitting Applications. *Chem. Mater.* **2016**, *28*, 5621−5634.

(19) Qian, X.; He, J.; Mastronardo, E.; Baldassarri, B.; Yuan, W.; Wolverton, C.; Haile, S. M. Outstanding Properties and Performance of CaTi0.5Mn0.5O3−δ for Solar-Driven Thermochemical Hydrogen Production. *Matter* **2021**, *4*, 688−708.

(20) McDaniel, A. H.; Miller, E. C.; Arifin, D.; Ambrosini, A.; Coker, E. N.; O'Hayre, R.; Chueh, W. C.; Tong, J. Sr- and Mn-Doped LaAlO3−δ for Solar Thermochemical H2 and CO Production. *Energy Environ. Sci.* **2013**, *6*, 2424−2428.

(21) Chen, Z.; Jiang, Q.; Cheng, F.; Tong, J.; Yang, M.; Jiang, Z.; Li, C. Sr- and Co-Doped LaGaO3−δ with High O2 and H2 Yields in Solar Thermochemical Water Splitting. *J. Mater. Chem. A* **2019**, *7*, 6099−6112.

(22) Wang, L.; Al-Mamun, M.; Liu, P.; Wang, Y.; Yang, H. G.; Zhao, H. La1−xCaxMn1−yAlyO3 Perovskites as Efficient Catalysts for Two-Step

Thermochemical Water Splitting in Conjunction with Exceptional Hydrogen Yields. *Chin. J. Catal.* **2017**, *38*, 1079−1086.

(23) Kubicek, M.; Bork, A. H.; Rupp, J. L. M. Perovskite Oxides-a Review on a Versatile Material Class for Solar-to-Fuel Conversion Processes. *J. Mater. Chem. A* **2017**, *5*, 11983.

(24) Barcellos, R. D.; Sanders, M. D.; Tong, J.; McDaniel, A. H.; O'Hayre, R. P. BaCe$_{0.25}$Mn$_{0.75}$O$_{3-\delta}$ - Promising Perovskite-Type Oxide for Solar Thermochemical Hydrogen Production. *Energy Environ. Sci.* **2018**, *11*, 3256−3265.

(25) Park, J. E.; Bare, Z. J. L.; Morelock, R. J.; Rodriguez, M. A.; Ambrosini, A.; Musgrave, C. B.; McDaniel, A. H.; Coker, E. N. Computationally Accelerated Discovery and Experimental Demonstration of Gd$_{0.5}$La$_{0.5}$Co$_{0.5}$Fe$_{0.5}$O$_3$ for Solar Thermochemical Hydrogen Production. *Front. Energy Res* **2021**, *9*, No. 750600.

(26) Orfila, M.; Linares, M.; Pérez, A.; Barras-García, I.; Molina, R.; Marugán, J.; Botas, J. A.; Sanz, R. Experimental Evaluation and Energy Analysis of a Two-Step Water Splitting Thermochemical Cycle for Solar Hydrogen Production Based on La$_{0.8}$Sr$_{0.2}$CoO$_{3-\delta}$ Perovskite. *Int. J. Hydrogen Energy* **2022**, *47*, 41209−41222.

(27) Wang, L.; Al-Mamun, M.; Zhong, Y. L.; Liu, P.; Wang, Y.; Yang, H. G.; Zhao, H. Enhanced Thermochemical Water Splitting through Formation of Oxygen Vacancy in La$_{0.6}$Sr$_{0.4}$BO$_{3-\delta}$ (B=Cr, Mn, Fe, Co, and Ni) Perovskites. *ChemPlusChem* **2018**, *83*, 924−928.

(28) Pérez, A.; Orfila, M.; Linares, M.; Sanz, R.; Marugán, J.; Molina, R.; Botas, J. A. Hydrogen Production by Thermochemical Water Splitting with La$_{0.8}$Al$_{0.2}$MeO$_{3-\delta}$ (Me= Fe, Co, Ni and Cu) Perovskites Prepared under Controlled pH. *Catal. Today* **2022**, *390-391*, 22−33.

(29) Demont, A.; Abanades, S.; Beche, E. Investigation of Perovskite Structures as Oxygen-Exchange Redox Materials for Hydrogen Production from Thermochemical Two-Step Water-Splitting Cycles. *J. Phys. Chem. C* **2014**, *118*, 12682−12692.

(30) Haeussler, A.; Julbe, A.; Abanades, S. Investigation of Reactive Perovskite Materials for Solar Fuel Production via Two-Step Redox Cycles: Thermochemical Activity Thermodynamic Properties and Reduction Kinetics. *Mater. Chem. Phys.* **2022**, *276*, No. 125358.

(31) Wang, L.; Al-Mamun, M.; Liu, P.; Wang, Y.; Yang, H. G.; Zhao, H. Notable Hydrogen Production on La$_x$Ca$_{1-x}$CoO$_3$ Perovskites via Two-Step Thermochemical Water Splitting. *J. Mater. Sci.* **2018**, *53*, 6796−6806.

(32) Dey, S.; Naidu, B. S.; Govindaraj, A.; Rao, C. N. R. Noteworthy Performance of La$_{1-x}$Ca$_x$MnO$_3$ Perovskites in Generating H$_2$ and CO by the Thermochemical Splitting of H$_2$O and CO$_2$. *Phys. Chem. Chem. Phys.* **2015**, *17*, 122−125.

(33) Carrillo, R. J.; Hill, C. M.; Warren, K. J.; Scheffe, J. R. Oxygen Nonstoichiometry and Defect Equilibria of Yttrium Manganite Perovskites with Strontium A-Site and Aluminum B-Site Doping. *J. Phys. Chem. C* **2020**, *124*, 4448−4458.

(34) Trindell, J. A.; Mcdaniel, A. H.; Ogitsu, T.; Ambrosini, A.; Sugar, J. D. Probing Electronic and Structural Transformations during Thermal Reduction of the Promising Water Splitting Perovskite BaCe$_{0.25}$Mn$_{0.75}$O$_3$. *Chem. Mater.* **2022**, *34*, 7712−7720.

(35) Rost, C. M.; Sachet, E.; Borman, T.; Moballegh, A.; Dickey, E. C.; Hou, D.; Jones, J. L.; Curtarolo, S.; Maria, J. P. Entropy-Stabilized Oxides. *Nat. Commun.* **2015**, *6*, 8485.

(36) Harrington, T. J.; Gild, J.; Sarker, P.; Toher, C.; Rost, C. M.; Dippo, O. F.; McElfresh, C.; Kaufmann, K.; Marin, E.; Borowski, L.; Hopkins, P. E.; Luo, J.; Curtarolo, S.; Brenner, D. W.; Vecchio, K. S. Phase Stability and Mechanical Properties of Novel High Entropy Transition Metal Carbides. *Acta Mater.* **2019**, *166*, 271−280.

(37) Jiang, S.; Hu, T.; Gild, J.; Zhou, N.; Nie, J.; Qin, M.; Harrington, T.; Vecchio, K.; Luo, J. A New Class of High-Entropy Perovskite Oxides. *Scr. Mater.* **2018**, *142*, 116−120.

(38) Gild, J.; Samiee, M.; Braun, J. L.; Harrington, T.; Vega, H.; Hopkins, P. E.; Vecchio, K.; Luo, J. High-Entropy Fluorite Oxides. *J. Eur. Ceram. Soc.* **2018**, *38*, 3578−3584.

(39) Zhang, K.; Li, W.; Zeng, J.; Deng, T.; Luo, B.; Zhang, H.; Huang, X. Preparation of (La$_{0.2}$Nd$_{0.2}$Sm$_{0.2}$Gd$_{0.2}$Yb$_{0.2}$)$_2$Zr$_2$O$_7$ High-Entropy Transparent Ceramic Using Combustion Synthesized Nanopowder. *J. Alloys Compd.* **2020**, *817*, No. 153328.

(40) Zhao, Z.; Chen, H.; Xiang, H.; Dai, F. Z.; Wang, X.; Xu, W.; Sun, K.; Peng, Z.; Zhou, Y. High Entropy Defective Fluorite Structured Rare-Earth Niobates and Tantalates for Thermal Barrier Applications. *J. Adv. Ceram.* **2020**, *9*, 303−311.

(41) Gild, J.; Zhang, Y.; Harrington, T.; Jiang, S.; Hu, T.; Quinn, M. C.; Mellor, W. M.; Zhou, N.; Vecchio, K.; Luo, J. High-Entropy Metal Diborides: A New Class of High-Entropy Materials and a New Type of Ultrahigh Temperature Ceramics. *Sci. Rep.* **2016**, *6*, 37946.

(42) Yan, X.; Constantin, L.; Lu, Y.; Silvain, J. F.; Nastasi, M.; Cui, B. (Hf$_{0.2}$Zr$_{0.2}$Ta$_{0.2}$Nb$_{0.2}$Ti$_{0.2}$)C High-Entropy Ceramics with Low Thermal Conductivity. *J. Am. Ceram. Soc.* **2018**, *101*, 4486−4491.

(43) Gild, J.; Braun, J.; Kaufmann, K.; Marin, E.; Harrington, T.; Hopkins, P.; Vecchio, K.; Luo, J. A High-Entropy Silicide: (Mo$_{0.2}$Nb$_{0.2}$Ta$_{0.2}$Ti$_{0.2}$W$_{0.2}$)Si$_2$. *J. Mater.* **2019**, *337*−343.

(44) Zhai, S.; Rojas, J.; Ahlborg, N.; Lim, K.; Toney, M. F.; Jin, H.; Chueh, W. C.; Majumdar, A. The Use of Poly-Cation Oxides to Lower the Temperature of Two-Step Thermochemical Water Splitting. *Energy Environ. Sci.* **2018**, *11*, 2172−2178.

(45) Wright, A. J.; Wang, Q.; Huang, C.; Nieto, A.; Chen, R.; Luo, J. From High-Entropy Ceramics to Compositionally-Complex Ceramics: A Case Study of Fluorite Oxides. *J. Eur. Ceram. Soc.* **2020**, *40*, 2120−2129.

(46) Wright, A. J.; Luo, J. A Step Forward from High-Entropy Ceramics to Compositionally Complex Ceramics: A New Perspective. *J. Mater. Sci.* **2020**, *55*, 8812−9827.

(47) Wright, A. J.; Wang, Q.; Ko, S.-T.; Chung, K. M.; Chen, R.; Luo, J. Size Disorder as a Descriptor for Predicting Reduced Thermal Conductivity in Medium- and High-Entropy Pyrochlores. *Scr. Mater.* **2020**, *76*−81.

(48) Wright, A. J.; Wang, Q.; Hu, C.; Yeh, Y.-T.; Chen, R.; Luo, J. Single-Phase Duodenary High-Entropy Fluorite/Pyrochlore Oxides with an Order-Disorder Transition. *Acta Mater.* **2021**, *211*, No. 116858.

(49) Qian, X.; He, J.; Mastronardo, E.; Baldassarri, B.; Wolverton, C.; Haile, S. M. Favorable Redox Thermodynamics of SrTi$_{0.5}$Mn$_{0.5}$O$_{3-\delta}$ in Solar Thermochemical Water Splitting. *Chem. Mater.* **2020**, *32*, 9335−9346.

(50) Takacs, M.; Scheffe, J. R.; Steinfeld, A. Oxygen Nonstoichiometry and Thermodynamic Characterization of Zr Doped Ceria in the 1573-1773 K Temperature Range. *Phys. Chem. Chem. Phys.* **2015**, *17*, 7813−7822.

(51) Scheffe, J. R.; Weibel, D.; Steinfeld, A. Lanthanum-Strontium-Manganese Perovskites as Redox Materials for Solar Thermochemical Splitting of H$_2$O and CO$_2$. *Energy Fuels* **2013**, *27*, 4250−4257.

(52) Sharan, A.; Lany, S. Computational Discovery of Stable and Metastable Ternary Oxynitrides. *J. Chem. Phys.* **2021**, *154*, 234706.

(53) Joubert, D. From Ultrasoft Pseudopotentials to the Projector Augmented-Wave Method. *Phys. Rev. B* **1999**, *59*, 1758−1775.

(54) Perdew, J. P.; Burke, K.; Ernzerhof, M. Generalized Gradient Approximation Made Simple. *Phys. Rev. Lett.* **1996**, *77*, 3865−3868.

(55) Brown, I. D.; Shannon, R. D. Empirical Bond-strength−Bond-length Curves for Oxides. *Acta Crystallogr. Sect. A* **1973**, *29*, 266−282.

(56) Brown, I. D. Recent Developments in the Methods and Applications of the Bond Valence Model. *Chem. Rev.* **2009**, *109*, 6858−6919.

(57) Shannon, R. D. Revised Effective Ionic Radii and Systematic Studies of Interatomic Distances in Halides and Chalcogenides. *Acta Crystallogr., Sect. A: Cryst. Phys., Diffr., Theor. Gen. Crystallogr.* **1976**, *A32*, 751−767.

(58) Hou, X.; Ohta, K.; Kimura, Y.; Tamenori, Y.; Tsuruta, K.; Amezawa, K.; Nakamura, T. Lattice Oxygen Instability in Oxide-Based Intercalation Cathodes: A Case Study of Layered LiNi$_{1/3}$Co$_{1/3}$Mn$_{1/3}$O$_2$. *Adv. Energy Mater.* **2021**, *11*, 2101005.

(59) Zuev, A. Y.; Vylkov, A. I.; Petrov, A. N.; Tsvetkov, D. S. Defect Structure and Defect-Induced Expansion of Undoped Oxygen Deficient Perovskite LaCoO$_{3-\delta}$. *Solid State Ionics* **2008**, *179*, 1876−1879.

(60) Vieten, J.; Bulfin, B.; Call, F.; Lange, M.; Schmücker, M.; Francke, A.; Roeb, M.; Sattler, C. Perovskite Oxides for Application in

Thermochemical Air Separation and Oxygen Storage. *J. Mater. Chem. A* **2016**, *4*, 13652−13659.

(61) Sanders, M. D.; Bergeson-Keller, A. M.; Coker, E. N.; O'Hayre, R. P. A Thermogravimetric Temperature-Programmed Thermal Redox Protocol for Rapid Screening of Metal Oxides for Solar Thermochemical Hydrogen Production. *Front. Energy Res.* **2022**, *10*, No. 856943.

(62) Crumlin, E. J.; Mutoro, E.; Hong, W. T.; Biegalski, M. D.; Christen, H. M.; Liu, Z.; Bluhm, H.; Shao-Horn, Y. In Situ Ambient Pressure X-Ray Photoelectron Spectroscopy of Cobalt Perovskite Surfaces under Cathodic Polarization at High Temperatures. *J. Phys. Chem. C* **2013**, *117*, 16087−16094.

(63) Niania, M.; Podor, R.; Britton, T. B.; Li, C.; Cooper, S. J.; Svetkov, N.; Skinner, S.; Kilner, J. *In Situ* Study of Strontium Segregation in La$_{0.6}$Sr$_{0.4}$Co$_{0.2}$Fe$_{0.8}$O$_{3−\delta}$ in Ambient Atmospheres Using High-Temperature Environmental Scanning Electron Microscopy. *J. Mater. Chem. A* **2018**, *6*, 14120−14135.

(64) Jung, W.; Tuller, H. L. Investigation of Surface Sr Segregation in Model Thin Film Solid Oxidefuel Cell Perovskite Electrodes. *Energy Environ. Sci.* **2012**, *5*, 5370−5378.

(65) Lukashuk, L.; Yigit, N.; Rameshan, R.; Kolar, E.; Teschner, D.; Hävecker, M.; Knop-Gericke, A.; Schlögl, R.; Föttinger, K.; Rupprechter, G. Operando Insights into CO Oxidation on Cobalt Oxide Catalysts by NAP-XPS, FTIR, and XRD. *ACS Catal.* **2018**, *8*, 8630−8641.

(66) Guse, K.; Papp, H. XPS Characterization of the Reduction and Synthesis Behaviour of Co/Mn Oxide Catalysts for Fischer-Tropsch Synthesis. *Fresenius' J. Anal. Chem.* **1993**, *346*, 84−91.

(67) Lukashuk, L.; Föttinger, K.; Kolar, E.; Rameshan, C.; Teschner, D.; Hävecker, M.; Knop-Gericke, A.; Yigit, N.; Li, H.; McDermott, E.; Stöger-Pollach, M.; Rupprechter, G. Operando XAS and NAP-XPS Studies of Preferential CO Oxidation on Co$_3$O$_4$ and CeO$_2$-Co$_3$O$_4$ Catalysts. *J. Catal.* **2016**, *344*, 1−15.

(68) Scheffe, J. R.; McDaniel, A. H.; Allendorf, M. D.; Weimer, A. W. Kinetics and Mechanism of Solar-Thermochemical H$_2$ Production by Oxidation of a Cobalt Ferrite-Zirconia Composite. *Energy Environ. Sci.* **2013**, *6*, 963−973.

(69) Chen, Z.; Jiang, Q.; Tong, J.; Yang, M.; Jiang, Z.; Li, C. Enhancement Effects of Dopants and SiO$_2$ Support on Mixed Metal Ferrites Based Two-Step Thermochemical Water Splitting. *Sol. Energy* **2017**, *144*, 643−659.

(70) Davenport, T. C.; Kemei, M.; Ignatowich, M. J.; Haile, S. M. Interplay of Material Thermodynamics and Surface Reaction Rate on the Kinetics of Thermochemical Hydrogen Production. *Int. J. Hydrogen Energy* **2017**, *42*, 16932−16945.

(71) Qi, H.; Lee, Y. L.; Yang, T.; Li, W.; Li, W.; Ma, L.; Hu, S.; Duan, Y.; Hackett, G. A.; Liu, X. Positive Effects of H$_2$O on the Hydrogen Oxidation Reaction on Sr$_2$Fe$_{1.5}$Mo$_{0.5}$O$_{6-\delta}$-Based Perovskite Anodes for Solid Oxide Fuel Cells. *ACS Catal.* **2020**, *10*, 5567−5578.

(72) Cao, Y.; Gadre, M. J.; Ngo, A. T.; Adler, S. B.; Morgan, D. D. Factors Controlling Surface Oxygen Exchange in Oxides. *Nat. Commun.* **2019**, *10*, 1346.

(73) Bulfin, B.; Miranda, M.; Steinfeld, A. Performance Indicators for Benchmarking Solar Thermochemical Fuel Processes and Reactors. *Front. Energy Res.* **2021**, *9*, No. 677980.

(74) Patel, R. K.; Ojha, S. K.; Kumar, S.; Saha, A.; Mandal, P.; Freeland, J. W.; Middey, S. Epitaxial Stabilization of Ultra Thin Films of High Entropy Perovskite. *Appl. Phys. Lett.* **2020**, *116*, No. 071601.

(75) Sarkar, A.; Wang, Q.; Schiele, A.; Chellali, M. R.; Bhattacharya, S. S.; Wang, D.; Brezesinski, T.; Hahn, H.; Velasco, L.; Breitung, B. High-Entropy Oxides: Fundamental Aspects and Electrochemical Properties. *Adv. Mater.* **2019**, *31*, 1806236.

(76) Sarkar, A.; Djenadic, R.; Wang, D.; Hein, C.; Kautenburger, R.; Clemens, O.; Hahn, H. Rare Earth and Transition Metal Based Entropy Stabilised Perovskite Type Oxides. *J. Eur. Ceram. Soc.* **2018**, *38*, 2318−2327.

(77) Li, Z.; Guan, B.; Xia, F.; Nie, J.; Li, W.; Ma, L.; Li, W.; Zhou, L.; Wang, Y.; Tian, H.; Luo, J.; Chen, Y.; Frost, M.; An, K.; Liu, X. High-Entropy Perovskite as a High-Performing Chromium-Tolerant

Cathode for Solid Oxide Fuel Cells. *ACS Appl. Mater. Interfaces* **2022**, *14*, 24363−24373.

(78) Ma, Y.; Ma, Y.; Wang, Q.; Schweidler, S.; Botros, M.; Fu, T.; Hahn, H.; Brezesinski, T.; Breitung, B. High-Entropy Energy Materials: Challenges and New Opportunities. *Energy Environ. Sci.* **2021**, *14*, 2883−2905.

(79) Wang, Q.; Sarkar, A.; Wang, D.; Velasco, L.; Azmi, R.; Bhattacharya, S. S.; Bergfeldt, T.; Düvel, A.; Heitjans, P.; Brezesinski, T.; Hahn, H.; Breitung, B. Multi-Anionic and -Cationic Compounds: New High Entropy Materials for Advanced Li-Ion Batteries. *Energy Environ. Sci.* **2019**, *12*, 2433−2442.

(80) Wang, J.; Cao, Z.; Zhu, X.; Yang, W. Improving Intermediate-Temperature Stability of BSCF by Constructing High Entropy Perovskites. *J. Membr. Sci. Lett.* **2022**, *2*, No. 100026.

(81) Mahon, H.; O'Connor, D.; Friedrich, D.; Hughes, B. A Review of Thermal Energy Storage Technologies for Seasonal Loops. *Energy* **2022**, *239*, No. 122207.

(82) Kuravi, S.; Trahan, J.; Goswami, D. Y.; Rahman, M. M.; Stefanakos, E. K. Thermal Energy Storage Technologies and Systems for Concentrating Solar Power Plants. *Prog. Energy Combust. Sci.* **2013**, *39*, 285−319.

(83) Khan, M. I.; Asfand, F.; Al-Ghamdi, S. G. Progress in Research and Technological Advancements of Thermal Energy Storage Systems for Concentrated Solar Power. *J. Energy Storage* **2022**, *55*, No. 105860.

(84) Ash-Kurlander, U.; Martin, O.; Fontana, L. D.; Patil, V. R.; Bernegger, M.; Mondelli, C.; Pérez-Ramírez, J.; Steinfeld, A. Impact of Daily Startup-Shutdown Conditions on the Production of Solar Methanol over a Commercial Cu-ZnO-Al$_2$O$_3$ Catalyst. *Energy Technol.* **2016**, *4*, 565−572.

(85) Mcdaniel, A. H.; Bell, R.; Martinek, J.; Ginley, D. *Initiating a Roadmap for Solar Fuels R & D : Imagining Beyond Thermochemical Cycles.Sandia Report SAND2022−7670,.* 2022.

(86) Li, W.; Jiang, N.; Hu, B.; Liu, X.; Song, F.; Han, G.; Jordan, T. J.; Hanson, T. B.; Liu, T. L.; Sun, Y. Electrolyzer Design for Flexible Decoupled Water Splitting and Organic Upgrading with Electron Reservoirs. *Chem* **2018**, *4*, 637−649.

(87) King, L. A.; Hubert, M. K. A.; Capuano, C.; Manco, J.; Danilovic, N.; Valle, E.; Hellstern, T. R.; Ayers, K.; Jaramillo, T. F. A Non-Precious Metal Hydrogen Catalyst in a Commercial Polymer Electrolyte Membrane Electrolyser. *Nat. Nanotechnol.* **2019**, *14*, 1071−1074.

(88) Weiß, A.; Siebel, A.; Bernt, M.; Shen, T.-H.; Tileli, V.; Gasteiger, H. A. Impact of Intermittent Operation on Lifetime and Performance of a PEM Water Electrolyzer. *J. Electrochem. Soc.* **2019**, *166*, F487−F497.

(89) Mallouk, T. E. Divide and Conquer. *Nat. Chem.* **2013**, *5*, 362−363.

(90) Mastronardo, E.; Qian, X.; Coronado, J. M.; Haile, S. M. The Favourable Thermodynamic Properties of Fe-Doped CaMnO$_3$ for Thermochemical Heat Storage. *J. Mater. Chem. A* **2020**, *8*, 8503−8517.

(91) Warren, K. J.; Tran, J. T.; Weimer, A. W. A Thermochemical Study of Iron Aluminate-Based Materials: A Preferred Class for Isothermal Water Splitting. *Energy Environ. Sci.* **2022**, *15*, 806−821.

(92) Qian, X.; Haile, S. M.; Davenport, T. C.; Mastronardo, E. Experimental Protocols for the Assessment of Redox Thermodynamics of Nonstoichiometric Oxides: A Case Study of YMnO$_{3-\delta}$. *J. Am. Ceram. Soc.* **2022**, *105*, 4375−4386.

(93) Mizusaki, J.; Mima, Y.; Shigeru, S.; And, Y.; Fuekir, K. Nonstoichiometry of the Perovskite-Type Oxides La$_{1-x}$Sr$_x$CoO$_{3-\delta}$. *J. Solid State Chem.* **1989**, *80*, 102−111.

(94) Takacs, M.; Hoes, M.; Caduff, M.; Cooper, T.; Scheffe, J. R.; Steinfeld, A. Oxygen Nonstoichiometry, Defect Equilibria, and Thermodynamic Characterization of LaMnO$_3$ Perovskites with Ca/Sr A-Site and Al B-Site Doping. *Acta Mater.* **2016**, *103*, 700−710.

(95) Hao, Y.; Yang, C. K.; Haile, S. M. Ceria-Zirconia Solid Solutions (Ce$_{1-x}$Zr$_x$O$_{2-\delta}$, x ≤ 0. 2) for Solar Thermochemical Water

Splitting: A Thermodynamic Study. *Chem. Mater.* **2014**, *26*, 6073−6082.

(96) Garnier, J. E.; Blumenthal, R. N.; Panlener, R. J.; Sharma, R. K. A Thermodynamic Study on CaO-Doped Nonstoichiometric Cerium Dioxide. *J. Phys. Chem. Solids* **1976**, *37*, 368−378.

(97) Ezbiri, M.; Takacs, M.; Theiler, D.; Michalsky, R.; Steinfeld, A. Tunable Thermodynamic Activity of $La_xSr_{1-x}Mn_yAl_{1-y}O_{3-\delta}$. *J. Mater. Chem. A* **2017**, *5*, 4172−4182.

(98) Ignatowich, M. J.; Bork, A. H.; Davenport, T. C.; Rupp, J. L. M.; Yang, C. K.; Yamazaki, Y.; Haile, S. M. Impact of Enhanced Oxide Reducibility on Rates of Solar-Driven Thermochemical Fuel Production. *MRS Commun.* **2017**, *7*, 873−878.

(99) Meredig, B.; Wolverton, C. First-Principles Thermodynamic Framework for the Evaluation of Thermochemical H_2O- or CO_2-Splitting Materials. *Phys. Rev. B* **2009**, *80*, No. 245119.

(100) Bakken, E.; Norby, T.; Stølen, S. Redox Energetics of Perovskite-Related Oxides. *J. Mater. Chem.* **2002**, *12*, 317−323.

(101) Wolverton, C.; Haile, S. HydroGEN Seedling : Transformative Materials for High- Efficiency Thermochemical Production of Solar Fuels, *DOE Hydrogen and Fuel Cells Annual Merit Review Proceedings (Project ID P167)*. Https://Www. Hydrogen.Energy.Gov/Pdfs/Review19/ P167_wolverton_2019_.2019.

(102) Naghavi, S. S.; Emery, A. A.; Hansen, H. A.; Zhou, F.; Ozolins, V.; Wolverton, C. Giant Onsite Electronic Entropy Enhances the Performance of Ceria for Water Splitting. *Nat. Commun.* **2017**, *8*, 285.

(103) Vieten, J.; Bulfin, B.; Huck, P.; Horton, M.; Guban, D.; Zhu, L.; Lu, Y.; Persson, K. A.; Roeb, M.; Sattler, C. Materials Design of Perovskite Solid Solutions for Thermochemical Applications. *Energy Environ. Sci.* **2019**, *12*, 1369−1384.

(104) Das, T.; Nicholas, J. D.; Qi, Y. Long-Range Charge Transfer and Oxygen Vacancy Interactions in Strontium Ferrite. *J. Mater. Chem. A* **2017**, *5*, 4493−4506.

(105) Marrocchelli, D.; Bishop, S. R.; Kilner, J. Chemical Expansion and Its Dependence on the Host Cation Radius. *J. Mater. Chem. A* **2013**, *1*, 7673−7680.

(106) Aidhy, D. S.; Liu, B.; Zhang, Y.; Weber, W. J. Chemical Expansion Affected Oxygen Vacancy Stability in Different Oxide Structures from First Principles Calculations. *Comput. Mater. Sci.* **2015**, *99*, 298−305.

(107) Gagné, O. C.; Hawthorne, F. C. Comprehensive Derivation of Bond-Valence Parameters for Ion Pairs Involving Oxygen. *Acta Crystallogr. Sect. B* **2015**, *71*, 562−578.

(108) Zoller, S.; Koepf, E.; Nizamian, D.; Stephan, M.; Patané, A.; Haueter, P.; Romero, M.; González-Aguilar, J.; Lieftink, D.; de Wit, E.; Brendelberger, S.; Sizmann, A.; Steinfeld, A. A Solar Tower Fuel Plant for the Thermochemical Production of Kerosene from H_2O and CO_2. *Joule* **2022**, *6*, 1606−1616.

📖 Recommended by ACS

Tunable Magnetic Transition Temperatures in Organic–Inorganic Hybrid Cobalt Chloride Hexagonal Perovskites

Teresa Lee, Robert J. Cava, *et al.*

FEBRUARY 15, 2023
CHEMISTRY OF MATERIALS　　READ 🔗

Suppression of Fe-Cation Migration by Indium Substitution in $LiFe_{2-x}In_xSbO_6$ Cathode Materials

Xabier Martínez de Irujo Labalde, Michael A. Hayward, *et al.*

DECEMBER 23, 2022
CHEMISTRY OF MATERIALS　　READ 🔗

Comprehensive Study of the Chemical, Physical, and Structural Evolution of Molecular Layer Deposited Alucone Films during Thermal Processing

Vamseedhara Vemuri, Nicholas C. Strandwitz, *et al.*

FEBRUARY 22, 2023
CHEMISTRY OF MATERIALS　　READ 🔗

Two Types of Negative Thermal Expansion Observed in $PbCr_{1-x}Ti_xO_3$

Yuki Sakai, Masaki Azuma, *et al.*

JANUARY 18, 2023
CHEMISTRY OF MATERIALS　　READ 🔗

Get More Suggestions >